Experimental and modeling investigation of thermal behaviour and performance of lithium ion prismatic cells at cold-start temperatures

by

Garrett Gauthier

A thesis
presented to the University of Waterloo
in fulfilment of the
thesis requirement for the degree of
Master of Applied Science
in
Mechanical and Mechatronics Engineering

Waterloo, Ontario, Canada, 2017

Author's Declaration

I hereby declare that I am the sole author of this thesis. This is a true copy of the thesis, including any required final revisions, as accepted by my examiners.

I understand that my thesis may be made electronically available to the public.

Abstract

In recent years, electric and hybrid-electric vehicles have been gaining market share as a viable and environmentally friendly alternative to conventional internal combustion engine vehicles, and an increasing number of long-range all-electric vehicles are becoming commercially available. The performance of these vehicles' batteries is strongly influenced by their operating temperature, which can vary significantly, not only over the course of a single drive, but also over the course of the vehicle's lifetime, particularly in regions with large seasonal temperature changes.

This thesis examines the thermal behaviour of $LiFePO_4$ cells and batteries and the influence of that behaviour on discharge performance under cold-start operating conditions representative of near- and sub-zero temperature driving. The first part of this thesis details the experimental characterization of global and local thermal behavior, and global voltage performance, of prismatic cells at ambient temperatures ranging from -10^oC to 12^oC. Characterization is performed on prismatic 20Ah $LiFePO_4$ batteries at discharge rates between 2C to 3C, under thermal conditions that both encourage and suppress temperature changes throughout the cell in order to examine the impacts of temperature variation, both spatially and temporally, on performance.

In the first instance, an insulated housing is constructed around the battery, minimizing heat transfer from the cell to the ambient. Under these conditions, and at low ambient temperatures, voltage drop is significant at the onset of discharge due to high impedance, and high charge transfer resistance in particular, and reaches as low as 2.74 V at 3C discharge. Thermally, mean cell temperature increases during the course of discharge, reaching a maximum at the end of discharge. The rate of temperature rise changes, however, over the course of discharge, corresponding to changes in charge transfer resistance, ohmic resistance, and mass transport resistance. Temperature rise is most rapid at the onset and end of discharge, corresponding to high charge transfer resistance and high cathode-side mass transport resistance, respectively. It is noted that as cell temperature rises, voltage temporarily increases or "recovers" despite the initial rapid drop at the onset of discharge, and that the magnitude of this recovery corresponds to the magnitude of temperature rise. It is seen that very similar discharge capacity is achieved regardless of discharge rate, demonstrating the tightly coupled feedback relationship between electrochemical and thermal behaviour. Discharge rate has a clear effect on temperature rise, with higher C-rates resulting in

greater cell impedance and therefore greater temperature rise. Spatially, it is observed that at 2C discharge, temperature rise is greatest near the centre of the cell and towards the positive terminal. As discharge rate increases, temperature rise at the positive terminal becomes increasingly dominant, with strong gradients forming in that region during 3C discharge. Maximum spatial temperature variation ranges from 2.9^{o}C at 2C discharge to 7.2^{o}C at 3C.

In the second characterization instance, the battery is discharged while submerged in a circulating water-ethylene glycol solution that rapidly transfers heat from the battery to the ambient. Under these conditions, spatial and temporal variation in cell temperature is minimal, and discharge voltage is observed to be very strongly dependent on ambient temperature, as cell temperature rise and voltage recovery are suppressed. In comparing discharge behaviour under such conditions with the earlier conditions described above, it is evident that a cell's generation of waste heat and the corresponding change in its internal operating temperature has a dramatic effect on moderating voltage loss at low temperatures. This observation also emphasizes the importance of heat transfer conditions in a battery's wider thermal environment on its performance.

The second part of this thesis applies the characterization data to validate a 0D lumped capacitance model and a 3D thermal-electrochemical coupled model of the cell. These models, available under the commercially-available simulation software AutoLion, are then used to investigate more specifically the influence of spatial thermal variations. The 0D model is shown to have good agreement at low temperatures and discharge rates, with generally poorer though still acceptable agreement as either temperature or discharge rate is increased. The 3D model, despite predicting an exaggerated voltage recovery effect, shows very good agreement in discharge capacity and temperature change. Model disagreements are attributed to 1) uncertainties in the coefficients of diffusion in the electrolyte and solid phases and their response to changes in temperature and lithium concentration; 2) the assumption of a constant SEI layer resistance that does not change with temperature; and 3) suspected inaccuracies in the distribution and magnitude of local charge density. The models are then applied to compare discharge behavior for thermally uniform and non-uniform cells under otherwise identical operating conditions. The results suggest that for thermally nonuniform cells operating at subzero ambient temperatures, the formation of temperature gradients, and therefore of areas of high and low local resistance, cannot be neglected for its influence on overall cell voltage. Moreover, the results are in contrast to commonly held

assumptions in the literature that a more thermally uniform cell should perform better and provide greater discharge capacity as a product of evenly distributed reactions across the electrode, consistent charge density, and uniform SOC. The findings provide insight into the significance of temperature gradients and their effects on prismatic battery performance under cold-start conditions, and illustrate the need to further refine models that are capable of describing the effects of these gradients under such conditions.

Acknowledgements

I would like to thank my supervisor, Dr. Xianguo Li, for providing guidance, support, and direction throughout my graduate studies. Your patience, understanding, and insight have been vital to the success of this research and my broader education.

I would also like to thank certain members of Dr. Li's research group: Kaiwei (Kevin) Chen, for investing significant efforts in mentoring and technical input throughout my research; Grant Unsworth for providing valuable assistance in experimental design and data interpretation; and Dr. Ibrahim Alaefour for review and feedback on writing style and presentation of results.

Dedication

To my parents and step-parents, for your endless support and encouragement. To my father, for fostering ambition and the drive to pursue it. To my mother, for teaching the balance between a firm rooting while embracing uncertainty. To my stepfather, for personifying steadfastness and discipline. And to my stepmother, for living a commitment to independence of thought and action.

And to Khary, for balancing broad perspective with relentless enthusiasm for the most delightful minutiae of life. Also for breakfast.

Table of Contents

List of Figures

List of Tables

1   Introduction

As the consequences of fossil fuel-based transportation on climate and air quality are increasingly understood and acknowledged, greater attention is being placed on the development and commercialization of hybrid electric vehicles (HEVs) and battery electric vehicles (BEVs). Industry has responded with several such vehicles from major manufacturers including Chevrolet, Ford, Nissan, Hyundai, and BMW, and with more boutique options available from conspicuous startup Tesla Motors. And within the political sphere, consumer acceptance of electric vehicles is being incentivized through the use of various subsidies and rebates [1].

Lithium ion (Li-ion) batteries are presently the leading candidate for energy storage in HEVs and BEVs due to their high energy and power density, high voltage, low self-discharge, and good stability [2]. However, Li-ion-powered vehicles operating in climates with below-freezing temperatures face unique challenges to their performance. The electrochemical and physicochemical processes occurring in Li-ion cells are highly temperature-dependent, and cells experience substantial losses in both power and capacity as temperature declines [2-6]. Addressing these losses is currently one of the highest priorities in Li-ion cell development [7, 8]. However, in order to optimize batteries and their thermal management systems for the full range of vehicle operating temperatures, a detailed understanding of the interplay between battery temperature, performance, and thermal response must be achieved.

1.1   Lithium Ion Batteries

A battery is a device that stores energy by means of electrochemical reactions. For automotive applications, desired traits in a battery include high energy and power density, long cycle life, low maintenance requirements, tolerance to repeated high power charges from regenerative braking, tolerance to high operating temperatures without thermal runaway reactions, and low cost [9]. Li-ion batteries are currently the favoured technology for automotive use due to their existing and further potential abilities to meet these requirements [7, 10]. The basic principles

of Li-ion batteries will be explored in the following subsection, followed by an overview of commercially available types of Li-ion batteries.

1.1.1 Electrochemical Mechanism of Lithium Ion Batteries

Li-ion batteries exploit the oxidation of lithium to generate an electric current. The battery consists of numerous adjacent cells, which in turn are composed of an anode and a cathode connected to electrically conductive current collectors and separated by an electronically insulating separator membrane. The anode, cathode, and separator are saturated with an ionically conductive electrolyte. The anode, or negative electrode, is the site at which lithium is oxidized to lithium ions (Li^+) during discharge, and is typically a graphitic carbon into and through which lithium particles can diffuse, or intercalate. Carbon materials are used for their ability to receive and release a large volume of lithium (Li:C=1:6) without changes to the anode's mechanical or electrical properties. The cathode, or positive electrode, is the site at which Li^+ is reduced to neutral lithium particles during discharge. It is typically a metal oxide with a layered, tunneled, or nano-particle structure that supports lithium intercalation with minimal resistance. The batteries used in this thesis use an iron phosphate nano-particle cathode.

When the battery is discharged, Li oxidizes to Li^+ at the anode and diffuses through the electrolyte to the cathode, where it is reduced to Li. The electrolyte, which consists of layers of ionically conductive and electrically non-conductive materials, serves to enable the transport of Li^+, and the separator layer prevents the transport of electrons between electrodes. Electrons flow from anode to cathode via current collector materials in contact with the electrodes and connected to an external circuit. In the case of the batteries used in this thesis, the anode-side current collector is made of copper and the cathode-side collector is aluminum.

For the LiFePO$_4$ cells used in this thesis, the chemical reaction during discharge can be described as follows:

$$\text{Negative reaction (anode):} \quad Li_xC_6 \leftrightharpoons C_6 + xLi^+ + xe^- \qquad (1.1)$$

$$\text{Positive reaction (cathode):} \quad Li_{1-x}FePO_4 + xLi^+ + xe^- \leftrightharpoons LiFePO_4 \qquad (1.2)$$

$$\text{Total reaction (whole cell):} \quad Li_{1-x}FePO_4 + Li_xC_6 \leftrightharpoons LiFePO_4 + C_6 \qquad (1.3)$$
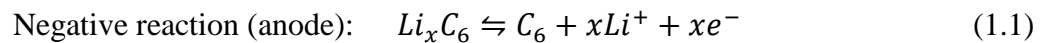
When the cell is connected to an external load and discharged, the spontaneous reaction is from left to right. Conversely, during charging, the reaction proceeds from right to left. The cell components and reaction described above are pictured in Figure 1.1.
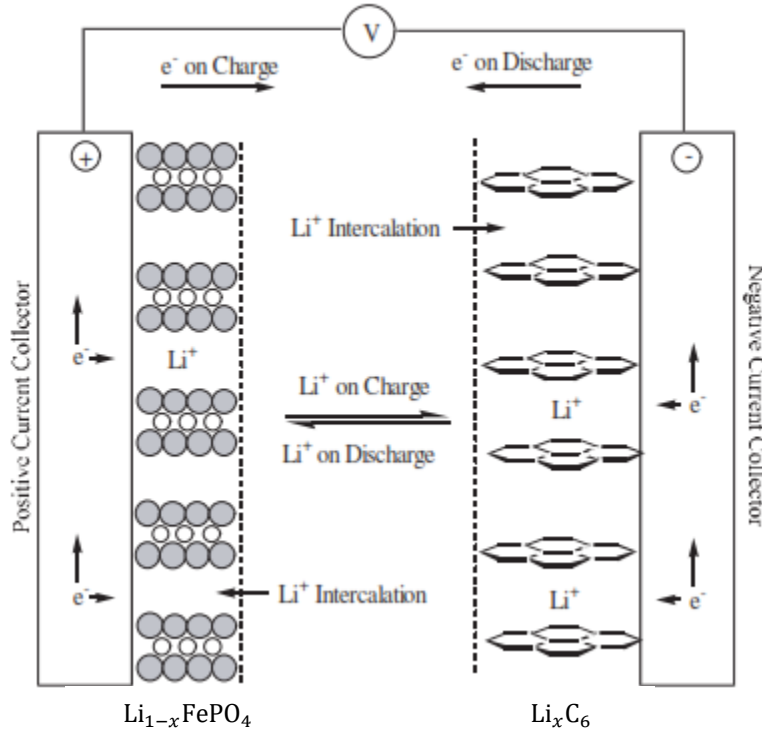
Figure 1.1: Schematic of cell components and reaction in a LiFePO₄ cell. Modified from [9].

The theoretical energy that can be obtained during discharge is defined by the change in the free energy of the cell, ΔG [9]:

$$\Delta G^{\circ} = -nFE^{\circ} \qquad (1.4)$$

where n is the number of electrons transferred in the reaction, F is the Faraday constant, and E° is the standard potential, or voltage, of the cell. The cell's standard potential is defined as the sum of the oxidation potential of the anode and the reduction potential of the cathode. It is dependent on the active materials used in the cell's design, and can vary significantly between different battery types.

In practice, the energy provided by a given cell during discharge is less than that indicated in equation 1.4. It is limited by irreversible losses, categorized as activation polarization, concentration polarization, and ohmic polarization. Activation polarization is due to limits to the rate of charge transfer at the electrodes. Concentration polarization arises due to limits to mass transfer of lithium through the cell. Ohmic polarization is a result of ohmic resistance to the flow of charged particles in the cell, and is a combination of the ionic resistance of the electrolyte and the electrical resistance of the current conducting materials. These irreversible losses consume some of the cell's maximum available energy and convert it to waste heat.

The cell voltage after accounting for the above polarization effects can be expressed as

$$E = E_0 - [(\eta_{ct})_a + (\eta_c)_a] - [(\eta_{ct})_c + (\eta_c)_c] - IR_i \qquad (1.5)$$

where E_0 is the open-circuit voltage of the cell, $(\eta_{ct})_a$ and $(\eta_{ct})_c$ are the activation polarization at the anode and cathode, respectively, $(\eta_c)_a$ and $(\eta_c)_c$ are the concentration polarization at the anode and cathode, respectively, I is the operating current of the cell, and R_i is the internal or ohmic resistance of the cell. The effects of polarization on cell voltage are illustrated in Figure 1.2.
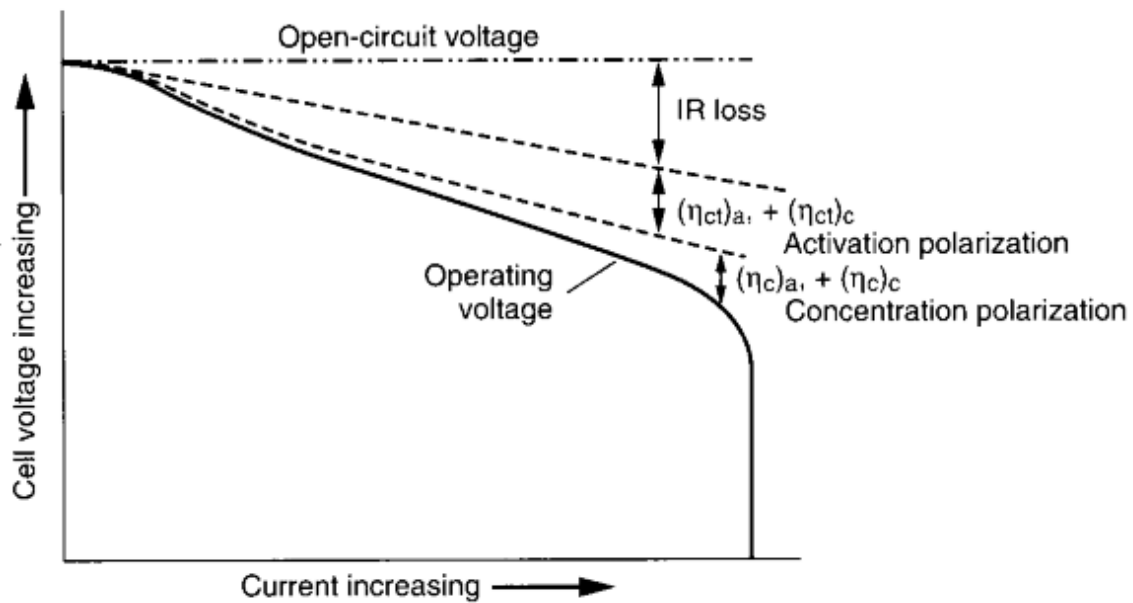
Figure 1.2: Cell voltage and polarization as a function of current [9].

The above discussion of cell voltage has assumed the cell and its active chemical species are at standard state conditions. In reality, a cell operating within an automotive battery system may deviate significantly from these conditions. Under these circumstances, the voltage can be expressed using the Nernst equation [9]:

$$E = E^0 - \frac{RT}{nF} \ln \frac{a_C^c a_D^d}{a_A^a a_B^b} \tag{1.6}$$

where R is the universal gas constant, T is absolute temperature, a_A^a and a_B^b are the chemical activities of the reactants at the anode and cathode, respectively, and a_C^c and a_D^d are the chemical activities of the products of oxidation and reduction at the anode and cathode, respectively. As can be seen in equation 1.6, the actual cell voltage depends both on the activities of the active species in the cell, which change during the course of discharge, as well as on cell operating temperature. As temperature changes, the cell voltage may increase or decrease, affecting the overall electrochemical performance of the battery system and therefore the performance of the vehicle itself.

A cell, however, is not a one-dimensional system, nor does it operate under constant temperature conditions during real-world driving conditions. It is three-dimensional, and its operating temperature varies spatially and over time, as will be described in Section 2. In order to design an optimal battery system to perform under realistic driving conditions, it is necessary to understand the effects of both spatial and temporal changes in cell temperature on its voltage behaviour.

1.1.2 Types of Lithium Ion Batteries

A lithium ion battery is a secondary, or rechargeable, battery which, as described above, uses the oxidation and reduction of lithium as its mechanism to release and store energy. Several types of Li-ion batteries have been developed for a range of applications, and differ notably in the materials and form factors used.

Li-ion batteries are typically named for the cathode material used. The first Li-ion batteries to be made commercially available were lithium cobalt oxide, or $LiCoO_2$. Since then, a number of other materials have been marketed, including manganese oxide ($LiMn_2O_4$) and nickel cobalt oxide ($LiNi_{1-x}Co_xO_2$) [9]. For this thesis, the batteries used are lithium iron phosphate ($LiFePO_4$) with a nominal capacity of 19.5 Ah, developed by A123 systems (A123M1HD-A). The $LiFePO_4$ chemistry is considered suitable for automotive applications due to its ability to support high rates of Li mass transport and therefore high discharge rates, as well as its safety; even at relatively high temperatures, the electrodes and electrolyte are not prone to secondary reactions which would lead to degradation or thermal runaway and fires [9].

Battery form factor also varies depending on the battery's chemistry and intended application. Cylindrical and coin batteries are commonly used in consumer electronics for which primary (non-rechargeable) cells are sufficient. Secondary cylindrical batteries have also been developed, including Li-ion chemistries, and have been used for EV applications. The batteries used in this thesis, however, are a prismatic type, with individual cells stacked in parallel. This form factor is common in existing EVs and HEVs due to its space-efficient geometry and because its high surface area-to-volume ratio is favourable for designing effective thermal management systems.

1.2   Motivation for This Work

Li-ion-powered vehicles operating in climates with below-freezing temperatures face unique challenges to their performance. The electrochemical and physicochemical processes occurring in Li-ion cells are highly temperature-dependent, and cells experience substantial losses in both power and capacity as temperature declines [2-6]. Addressing these losses is currently one of the highest priorities in Li-ion cell development [7, 8].

As discussed, the dominant factors responsible for low-temperature performance losses are generally understood to be 1) sluggish charge transfer kinetics at the electrodes (activation polarization), 2) poor rates of mass transport through various regions of the cell concentration polarization), and 3) resistance to electron transport through the current collector layers (ohmic

polarization). These sources of internal resistance affect a cell's behaviour not only by limiting its electrical performance, but also by influencing its internal heat generation. As a cell's operating temperature decreases, the corresponding rise in overall internal resistance results in greater heat generation, and cell temperature may increase depending on its operating conditions and external environment [2, 11, 12]. The process of cell self-heating is therefore a tightly coupled system of electrochemical and thermal feedback processes that promote heat generation during low-temperature operation and attenuate heat generation as temperature increases and electrochemical efficiency improves [2, 7]. The highest rates of heat generation during discharge have been observed at very high and very low state-of-charge (SOC), corresponding to high charge transfer resistance and cathode-side diffusion resistance, respectively [2, 13]. Additionally, while ohmic resistance may not be a dominant contributor to cell impedance at low temperatures, its contribution to heat generation can be substantial, particularly in the large prismatic cells employed in EVs and HEVs. The high specific power and specific energy of these cells enable high discharge current densities, and their geometries favour edge current collection, resulting in especially high current density near the terminals. Consequently, prismatic cells can exhibit significant ohmic losses and Joule heating at the terminals, to an extent that is not apparent in smaller cylindrical and coin cells [14-17].

Large prismatic cells are therefore especially prone to the formation of large spatial temperature gradients. The effects of thermal non-uniformity on cell voltage and effective capacity, however, are not yet well understood. Numerical modeling approaches have been developed to predict thermal and electrochemical cell behaviour under a range of operating conditions. Initially, such models simplified the cell to a one-dimensional electrochemical system with a lumped capacitance, or 0D, thermal model that represents temperature as uniform over the entire cell. However, more recently developed models have expanded to multi-dimensional electrochemical and thermal models, and the results highlight the limitations of 0D modeling under low-temperature conditions, as such conditions promote thermal non-uniformities that cannot be adequately represented by lumped capacitance models.

In order to assess the applicability of fully 3D thermal-electrochemical modeling to prismatic cell operation at low temperatures, further validation is necessary. Despite the unique non-uniform thermal behaviour exhibited by prismatic cells, few experimental studies have

investigated their low-temperature performance, particularly at discharge rates representative of real-world driving. Furthermore, spatially-resolved temperature data under these conditions is presently unavailable for 3D modeling validation. Lastly, while the heat transfer coefficient between a cell and its surroundings is an important input for thermal models [18], heat transfer conditions are rarely reported in experimental studies of cell performance.

This thesis first details the experimental characterization of global and local thermal behavior, and global voltage performance, of prismatic cells at ambient temperatures ranging from -10°C to 12°C. Characterization is performed on prismatic 20Ah LiFePO$_4$ cells at discharge rates between 2C to 3C, under thermal conditions that both encourage and suppress temperature changes throughout the cell in order to examine the impacts of temperature variation, both spatially and temporally, on performance. Characterization results are then used to validate commercialized 3D and lumped capacitance models to assess the applicability of each model to prismatic batteries operating at cold-start temperatures, and identify specific areas for future improvement such models.

1.3   Objectives of This Work

The objectives of this thesis are as follows:

1. To achieve spatially-resolved thermal and voltage characterization of prismatic Li-ion battery behaviour during cold-start discharge. The results of this objective provide the necessary foundation of discharge behaviour data and observations on which the remaining objectives depend.
2. To investigate the applicability of a) a lumped capacitance, or 0D, thermal model; and b) a 3D thermal model to prismatic Li-ion batteries during cold-start operation. This objective seeks to ascertain whether more commonly-employed lumped capacitance models can accurately describe prismatic battery performance under cold-start conditions, and furthermore whether a 3D model can provide significant improvement and may therefore be warranted over its simplified counterpart.

3. To identify specific areas for improvement in a commercialized model for further refinement. This thesis applies an existing, commercially-available model software package capable of both lumped capacitance and 3D thermal modeling and assesses its strengths and weaknesses, with specific weaknesses identified for improvement.

4. To describe the influence of the presence or absence of temperature gradients on discharge voltage behaviour. Using the models validated and assessed in objectives 2 and 3, this thesis seeks to verify assumptions that are commonly held but difficult to demonstrate experimentally: that, all other factors being held constant, the presence or absence of local temperature minima and maxima across prismatic batteries should affect the battery's performance, and moreover that a thermally uniform battery should provide greater discharge capacity that a non-uniform battery.

1.4   Scope and Outline of This Thesis

It is the aim of this thesis to investigate the effects of thermal non-uniformity on cell performance and to assess the applicability of a lumped capacitance, or 0D, thermal model and a fully 3D thermally-coupled electrochemical model to prismatic Li-ion batteries operating at cold-start temperatures. This is accomplished specifically under low-temperature (-10 – 12°C) conditions, as the temperature-sensitivity of Li-ion cells is particularly evident under such conditions and because such conditions remain a limitation to EV performance goals.

First, experimental characterization of global and local thermal behavior, and global voltage performance, is undertaken under the aforementioned temperature conditions. Characterization is performed at discharge rates representative of real-world driving, under thermal conditions that both encourage and suppress temperature changes throughout the cell in order to examine the impacts of temperature variation, both spatially and temporally, on performance. Experimental methods are described in Section 3, and characterization results in Section 5.1.

Next, characterization data are used to validate a one-dimensional electrochemical with lumped capacitance thermal model, and a three-dimensional thermal-electrochemical model, of

the cell's thermal and voltage behaviour during discharge. The models are discussed in Section 4, and validation results are presented in Section 5.2. The validated models are then used to examine the suitability of each model in describing discharge behaviour under cold-start conditions and the effects of thermal non-uniformity on a cell's electrical performance under low-temperature conditions.

Finally, in Section 6, the key findings of this thesis are summarized, and recommendations for future research are presented.

2 Literature Review

Battery-powered vehicles operating in climates with below-freezing temperatures face unique challenges to their performance. The electrochemical and physicochemical processes occurring in Li-ion batteries are highly temperature-dependent, and cells experience substantial losses in both power and capacity as temperature declines. Addressing these losses is currently one of the highest priorities in their development [7], and the U.S. Department of Energy (USDOE) has set long-term industry targets for cold-cranking power and minimum operating temperature [8], as shown in Table 2.1. Effective thermal management of battery systems is therefore a crucial component of electric vehicle (EV) development.

Table 2.1: Summary of USDOE FreedomCAR energy storage goals for HEVs [8].

Characteristics	Units	Requirements	
		Minimum	Maximum
Peak discharge pulse power (10 s)	kW	25	40
Peak regenerative pulse power (10 s)	kW	20	35
Total available energy	kWh	300	500
Cold cranking power at -30°C	kW	5	7
Calendar life	years	15	
Maximum weight	kg	40	60
Maximum volume	L	32	45
Operation temperature range	^{o}C	-30	52
Survival temperature range	^{o}C	-46	66

To achieve effective thermal management of Li-ion battery systems, the thermal behaviour of Li-ion cells should first be well understood, both temporally and spatially, during sub-zero discharge. Once the mechanisms that govern interactions between cell temperature and electrochemical and physicochemical processes are reasonably understood, models can be developed to aid in the design of thermal management solutions. The following sections review the thermal and chemical interactions that occur in Li-ion cells at low temperatures, followed by the efforts made to model those interactions.

2.1   Temperature Effects in Lithium Ion Batteries

Significant losses in cell power and capacity during low-temperature operation have been widely documented for a variety of Li-ion cell types [2-6, 19, 20], and these losses remain a major limitation to cell performance in vehicular and other applications [5].

Nagasubramanian [3] reported 95% loss in energy density and 99% loss in power density for cylindrical 18650 cells when temperature was decreased from 25°C to -40°C. The authors attributed these losses to greater cell impedance at lower temperatures, as measured impedance increased by an order of magnitude over the same temperature range. The response of individual sources of internal resistance to temperature, however, was seen to vary. Charge transfer resistance and resistance at the solid electrolyte interface (SEI) layer on the cathode side dominated, while ohmic resistance was minimal and nearly constant across all temperatures.

SEI resistance can be attributed to lithium diffusion rates; as temperature decreases, the kinetic energy of cyclable lithium declines, and diffusion across the cell layers is impeded. Andre et al. [6] showed that poor diffusion at low temperatures creates strong resistance to mass transport at the SEI, where lithium intercalation occurs, as well as within the electrolyte layer. Additional studies, both experimental [21-23] and numerical [11, 12], highlighted the electrolyte layer, citing greatly reduced ionic conductivity as a cause of poor low-temperature performance. A third notable source of mass transport resistance occurs due to poor solid-state diffusion within the electrodes themselves, and likewise increases with decreasing temperature [24, 25].

12

Charge transfer resistance in particular, however, has been found to be especially sensitive to temperature. Zhang et al. [4, 19] found that charge transfer resistance increases exponentially with decreasing temperature relative to a reference point of 20°C, and they and other authors [26-28] have demonstrated that it dominates all other resistances at temperatures below -10°C. The problem of poor low-temperature cell performance has therefore largely been attributed to electrode reaction kinetics.

The above findings were reinforced by Chen and Li [29], who observed a 95% loss in discharge capacity for large 20Ah prismatic cells when cell temperature was decreased from 20°C to -10°C. They highlighted the sensitivity of cell capacity to small changes in temperature; even at a near-optimal operating temperature [30] of 22°C, a 2°C drop in temperature produced a 2.3% drop in capacity [29]. Their work on accurate cell temperature control methods to account for a cell's own internal resistive heating suggests that the response of internal resistances, and therefore of cell performance, to temperature may be even more sensitive than previously indicated in prior experimental studies.

Table 2.2 summarizes the conditions and cell geometries for which low-temperature discharge performance has been examined. Note that investigations of prismatic cells are presently limited in number and scope.

While work remains to be done to better understand the exact mechanisms and relative importance of various internal resistances during low-temperature operation, the role of these resistances in heat generation has been widely acknowledged. Heat generation in batteries can be divided into a reversible component (entropic changes) and an irreversible component (resistive losses). Irreversible heat generation is highly sensitive to operating temperature, as it is composed of three fundamental temperature-dependent sources: charge-transfer or activation resistance, diffusion or mass transport resistance, and ohmic resistance or Joule heating [7].

Table 2.2: Summary of cell geometries and operating conditions employed in experimental studies of low-temperature lithium ion cell performance.

Author	Battery Geometry	Ambient Temperature(s) (°C)	Discharge Rate(s)
Chen and Li [29]	Prismatic	-10 – 40	C/5 – 3C
Awarke et al. [31]	Prismatic	-2	3C
Lin et al. [20]	Prismatic	-15 – 40	Unspecified
Nagasubramanian [3]	Cylindrical	-40 – 35	C/70 – 3C
Linden and Reddy [9]	Cylindrical	-20 – 20	C/14
Ji et al. [2]	Cylindrical	-20 – 45	1C – 4.6C
Andre et al. [6]	Cylindrical	-30 – 50	C/50 – 1C
Zhang et al. [4]	Experimental	-40 – 20	C/2

An expression for volumetric heat generation using a thermodynamic energy balance on a complete cell was developed by Bernardi et al. [32] and simplified by Gu and Wang [14], and has been applied extensively to a variety of battery models. The expression is given as follows:

$$q = i(U - V) - i\left(T\frac{\partial U}{\partial T}\right) \tag{2.1}$$

where q (J/m^3·s) is the volumetric heat generation rate, i (A/m^3) is the volumetric current density and is positive for discharge and negative for charging; U and V (V) are the open circuit voltage and instantaneous voltage, respectively; and T (K) is the cell temperature. The first term encompasses heat generation due to irreversible losses, as these losses are reflected in the

overpotential $(U - V)$ at a given cell temperature, while the second term describes entropic heating.

Although ohmic resistance may not be a dominant contributor to cell impedance at low temperatures, its contribution to total irreversible heating can nevertheless be substantial, particularly in the large prismatic cells employed in EVs. The high specific power and specific energy of prismatic cells enable high discharge current densities for long durations. In addition, the geometry of prismatic cells lends itself to edge current collection, resulting in especially high current density near the terminals. Consequently, these cells can experience significant ohmic losses and Joule heating at the current collectors, to an extent that is not apparent in smaller cylindrical and coin cells [14-17, 33]. To account for this additional Joule heating, an expression for volumetric heat generation has been developed specifically for prismatic cells [14, 34]:

$$q = aJ\left[U - V - T\frac{\partial U}{\partial T}\right] + a_p r_p i_n^2 + a_n r_n i_n^2 \tag{2.2}$$

$$\vec{i}_p = -\frac{1}{r_p}\nabla V_p \tag{2.3}$$

$$\vec{i}_n = -\frac{1}{r_n}\nabla V_n \tag{2.4}$$

where a (m^{-1}) is the specific area of the battery; J (A/m^2) is the current density; a_p and a_n (m^{-1}) are the specific areas of the positive and negative electrodes, respectively; $\vec{i}_p$ and $\vec{i}_n$ (A/m) are the current density vectors in the positive and negative electrodes, respectively; r_p and r_n (Ω) are the electrical or ohmic resistance in the positive and negative electrodes, respectively; and V_p and V_n (V) are the potential in the positive and negative electrodes, respectively. The third and fourth terms encompass the additional Joule heating at the electrodes.

Equations 2.1 – 2.4 are based on an energy balance being performed over an entire cell and assume a uniform cell temperature [14]. As discussed in Section 2.2 below, this assumption does not always hold, particularly for large form factor cells for which edge effects are not negligible, and more sophisticated expressions for heat generation have therefore been developed (see Section 4). However, for the purposes of the present discussion, the above equations illustrate the positive

15

relationship between internal resistance and heat generation, and several studies [2, 11, 12, 33] confirm that as cell temperature drops, the rate of heat generation increases. Chen et al. [33] developed a calorimeter for prismatic Li-ion cells and observed that at 1C discharge, the maximum rate of heat generation approximately tripled as cell temperature decreased from 40°C to -10°C when testing the same LiFePO4 cells used in this thesis. Arora et al. [35], in similar calorimetry experiments on prismatic cells of the same chemistry and capacity, observed more than a seven-fold increase in maximum heat generation when temperature dropped from 50°C to -10°C, at the same discharge rate of 1C.

A cell's self-heating behaviour can vary, however, depending on SOC and cell design. SOC influences cell impedance and thus affects the rate of heat generation. Specifically, the greatest heat generation during discharge is observed at very high and very low SOC, corresponding to high charge transfer resistance and cathode-side diffusion resistance, respectively [2, 13]. Chen et al. [33] demonstrated that the greatest rates of heat generation occur in the regions of the discharge curve where charge-transfer and mass transport resistances dominate, respectively, and reach a maximum at the end of discharge. Cell design considerations can alter both heat generation and heat dissipation rates; for example, the size and placement of current collectors will affect Joule heating [16], while geometry influences how effectively heat is dissipated [36]. In particular, the small cross-sectional area of prismatic cells, such as those used in this thesis, provides a large surface area-to-volume ratio that promotes heat dissipation to the ambient.

Lastly, it should be pointed out that as heat generation increases the temperature of a cell, impedance is reduced. The process of cell self-heating is therefore a tightly coupled system of electrochemical and thermal feedback processes that promote heat generation during low-temperature operation and attenuate heat generation as temperature increases and electrochemical efficiency improves [2, 7]. Electrochemical and thermal behaviour thus depends on cell design, operating temperature, and the heat transfer conditions within and surrounding the cell.

While the above review establishes the general effects of, and generation of, heat in lithium ion cells, it is important to recognize that thermal behaviour is not spatially uniform throughout a cell. Spatial considerations are discussed in the following section.

2.2 Temperature Distributions

The performance of a Li-ion cell can be influenced in part by two factors: the size and shape of its electrodes, and the size and placement of the current collectors. If an electrode design is sub-optimal, voltage and current density will be distributed non-uniformly, resulting in spatial variations in the utilization of the active material. Additionally, the voltage drop along the current collectors due to ohmic losses may be great enough to further affect current density distributions, with greater current density near the terminals [13, 16]. This localized active material utilization and inhomogeneous current density translates to spatial variations in charge-transfer and ohmic resistances, particularly during high-power discharge. Heat generated at points of high local impedance is conducted through the cell to areas of lower local temperature, producing temperature gradients over the reaction sites and forming a non-uniform distribution [37].

Studies of temperature distributions and their underlying mechanisms have been conducted at ambient temperatures ranging from -2 – 25°C, for discharge rates between 0.25 – 25C. For example, Keyser et al. [38] reported temperature gradients of 13.5^{o}C across prismatic cells undergoing 6C discharge, though the authors did not specify the ambient temperature. Local temperature was highest near the battery terminals, particularly near the positive electrode terminal. This thermal non-uniformity is attributed to the edge current collection design of prismatic cells, which results in high current density near the terminals and therefore in significant local ohmic resistance and joule heating. Due to the high ohmic resistivity of the aluminum positive electrode relative to the copper negative electrode, the greatest cell heating is observed near the positive electrode terminal. This pattern of terminal-dominated heat generation, pictured in Figure 2.1, has been demonstrated in additional studies, both experimental [13, 16] and numerical [16, 31].

Fleckenstein et al. [39] expanded on this work, identifying variations in local current density and local state of charge within cylindrical cells due to the presence of temperature gradients, with higher-temperature areas exhibiting greater current density and lower state of charge. For a maximum spatial temperature difference of 20°C between the hottest and coldest locations within a cell, local current density varied by 29% and local state of charge by 9%.
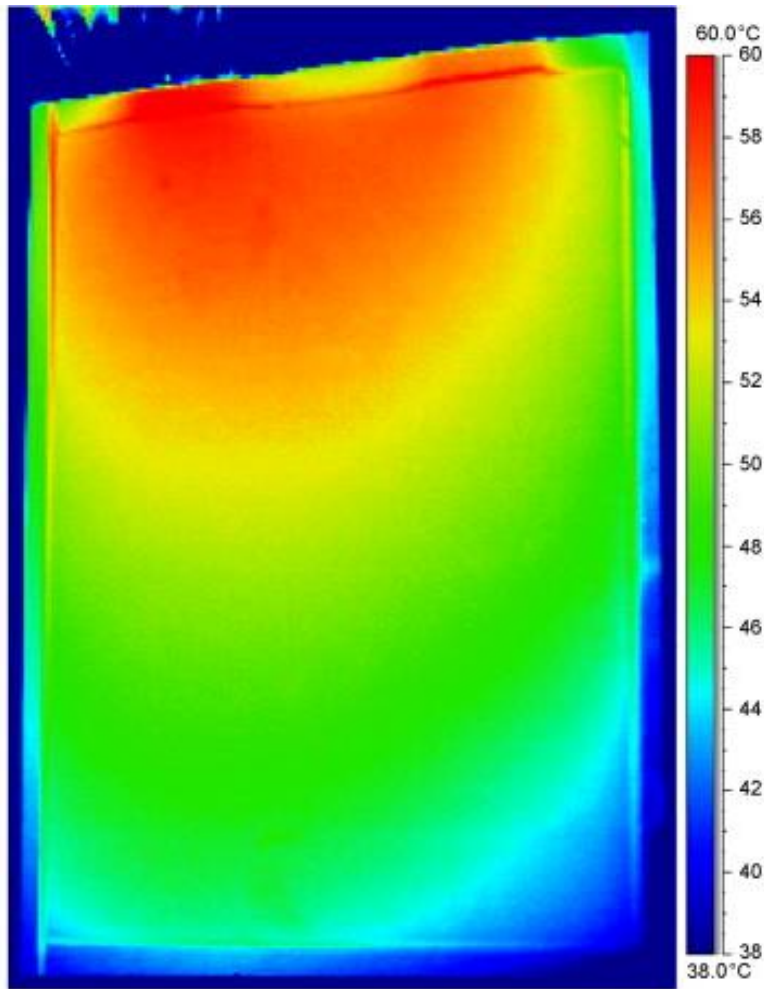
Figure 2.1: Infrared image of temperature distribution for a prismatic Li-ion cell after 5C discharge at room temperature [16].

These inhomogeneities in local thermal and electrochemical behaviour may have adverse effects on cell operation, as studies suggest that the presence of temperature gradients leads to accelerated cell aging and reduced cell lifespan [16, 36, 39]. This appears a particularly relevant challenge for large prismatic cells manufactured for EVs, as Kim et al. [16] demonstrated numerically that current density and temperature become increasingly non-uniform as a cell's electrode size, and therefore cell size, increases. A spatially-resolved understanding of the thermal behaviour of large-format prismatic cells is therefore of interest.

Table 2.3 summarizes the test conditions and results of experimental studies of temperature distributions. The largest variations in temperature are observed for very high discharge rates which are unrealistic under normal EV driving conditions. However, given the strong dependency of internal heat generation rates on cell temperature as discussed in the previous section, and the inhomogeneity of heat generation as discussed above, it can be expected that significant temperature gradients may develop for cells operating at low ambient temperatures, even for moderate discharge rates. Therefore, an investigation of spatial thermal behaviour is necessary at low temperatures if EV battery systems are to be optimized for cold-start, low-temperature driving conditions.

Table 2.3: Maximum spatial temperature variation observed during experimental discharge of Li-ion cells.

Author	Battery Geometry	Ambient Temperature(s) (ºC)	Discharge Rate(s)	Maximum Spatial Temperature Variation (ºC)
Kim et al. [16]	Prismatic	Room temperature	0.5C – 5C	23
Keyser et al. [38]	Prismatic	Unspecified	2C – 6C	13.5
Yang et al. [13]	Prismatic	25	1C – 25C	10.1
Awarke et al. [31]	Prismatic	-2	3C	1.9
Chen and Li [29]	Prismatic	20	0.25C – 3C	4.3
Inui et al. [36]	Prismatic	16	1C	3
	Cylindrical	16 – 22	0.5C – 1C	4
Fleckenstein et al. [39]	Cylindrical	5	5C – 8C	20

Additionally, it is worth noting that the cited experimental studies do not report the heat transfer conditions between the cell surface and its environment during testing, with the exception of Chen and Li [29]. Such conditions are required for validation of cell thermal and electrochemical models, as will be discussed in the following section.

2.3   Battery Models

Efforts to model the thermal and electrochemical behaviour of single cells and pack arrangements originated with the thermodynamic energy balance of a complete cell as developed by Bernardi et al. [32]. The full energy balance accounts for reversible (entropic) and irreversible (resistive losses) heating, as well as for the heat of mixing generated when current is interrupted and concentration gradients are permitted to relax [7].

Doyle et al. [40] subsequently proposed a 1D electrochemical model for a single cell based on concentrated solution theory, which treats gradients in electrochemical potential as the driving force for mass transport. Species and charge balances govern diffusion processes, while Butler-Volmer expressions model charge transfer kinetics at the SEI [41, 42].

Pals and Newman [11, 12] introduced a combined 1D electrochemical and thermal model based upon the fundamental work of Bernardi et al. [32] and Doyle et al. [40]. The model represents a thermally coupled approach to cell performance modeling, as cell temperature signals a feedback response in temperature-dependent electrochemical parameters (specifically, in electrolyte ionic conductivity and diffusion). These electrochemical changes alter the instantaneous voltage, resulting in changes to heat generation. The model assumes a constant current discharge, and simulations were performed only for isothermal and adiabatic cell conditions, limiting the applicability of results in investigations of EV battery performance involving complex drive cycles and thermal management systems.

More sophisticated electrochemical and thermal models based upon the work of Pals and Newman have been proposed. A large body of these mathematical models assumes one dimensional electrochemical gradients and provide only global values of cell characteristics such as current density, SOC, heat generation rate, and temperature [35, 39, 43, 44]. However, multi-

dimensional models have been developed to examine the development and effects of spatial inhomogeneities in cell performance.

Song and Evans [45] developed a thermally coupled model composed of Doyle et al.'s [40] 1D electrochemical model and the 2D heat transfer equation. Kwon et al. [46] proposed an electrochemical model to evaluate potential and current density in two dimensions; this approach was adapted by Kim et al. [15, 16] for a fully 2D electrochemical-thermal model specifically for large prismatic cells that accounts for potential drop along the length of the current collectors and the significant Joule heating that occurs in such cells. The model is thermally coupled in one direction, as local volumetric heat generation is treated as a function of local current production while electrochemical behaviour is temperature-independent.

Recently, Fan et al. [47] proposed a 2D electrochemical-thermal model for a cell undergoing relatively high rates of discharge (up to 2C) at temperatures as low as -10°C to represent cold-condition EV operation. Their electrochemical model accounts for the temperature-dependence of mass transport, as earlier described in part by Pals and Newman [11, 12], and of OCV. The model emphasizes the influence of large concentration gradients in the electrolyte that form during rapid discharge at low temperatures, and considers that electrolyte diffusion properties are concentration- and temperature-dependent and therefore change throughout the course of discharge.

A 2D thermal model by Chen and Evans [18] examined the significant effect that a model's heat transfer coefficient has on cell temperature both spatially and temporally. Their work highlights the importance of accurate determination of the heat transfer coefficient between a cell and its surroundings during experimental studies in order to enable validation of any thermal-electrochemical model. However, as mentioned in Section 2.2 above, it is not common practice to quantify the heat transfer conditions in experimental studies of cell thermal behaviour.

A notable limitation of 2D thermal-electrochemical models is that two dimensional approximations of three dimensional electrode geometries becomes less valid at the electrode corners, resulting in poor predictions of heat generation and temperature in these regions [16]. When a high degree of accuracy is required for spatially-resolved investigations, 3D approaches can be employed.

Gu and Wang [14] described a 3D fully coupled electrochemical-thermal model to simultaneously solve for the thermal energy balance and a number of temperature-dependent electrochemical and physicochemical properties, such as diffusion coefficients, ionic conductivity, and exchange current density. Its applicability can be extended to large prismatic cells with the inclusion of a Joule heating term in the solution for heat generation, in similar fashion to the 2D model by Kim et al. [16]. An extension of Gu and Wang's model is described in detail in Section 4.1.

Ji et al. [2] applied Gu and Wang's approach, albeit in simplified 1D form, in a study of low-temperature (-20°C) cell performance. The results closely matched experimental temperature and voltage measurements at low discharge rates (≤ 2C), suggesting effective thermal-electrochemical coupling, but exhibited significant overestimates in voltage and capacity at discharge rates exceeding 2C. As discussed in Section 2.2 above, high discharge current at low temperatures can induce substantial thermal inhomogeneities which in turn degrade cell performance. It is therefore likely that this 1D approach is insufficient to capture cell behaviour at low temperatures and realistic discharge rates for EVs. It remains to be seen whether a thermally coupled 3D model can successfully represent the inhomogeneous behaviour of prismatic cells at low temperatures.

A three dimensional, fully coupled model may be a valuable tool in evaluating and improving the low-temperature performance of large prismatic cells. Such a model should be validated experimentally to assess its applicability in research and development within the energy storage and EV sectors.

3   Experimental Setup

All discharge and thermal characterization tests are performed using commercially available lithium iron phosphate (LiFePO$_4$ or LFP) prismatic cells obtained from A123 Systems (AMP20M1HD-A). The cells have a nominal capacity of 19.5 Ah. Because new Li-ion cells may experience irreversible capacity fade during their initial discharge cycles, all cells have been subjected to an initial conditioning process of five C/3 discharge-charge cycles at an ambient temperature of 35°C [48].

Due to the inherent difficulty of measuring the internal temperature of a cell, and because the thickness of the cells used in the present study is two orders of magnitude less than their width and height, surface temperature is considered an acceptable measure of cell temperature [16]. This approach has the additional benefit of reducing all analysis of spatial thermal behaviour to two dimensions.

18 T-type thermocouples ($\pm$0.5°C) are mounted to the cell surface on each side with an epoxy. The thermocouple type and mounting method are consistent with the methods used by Chen and Li [29] in their study of prismatic Li-ion cell temperature control. The spatial arrangement of the thermocouples, illustrated in Figure 3.1, is a modification of that employed by Awarke et al. [31] in a previous study of temperature distributions in prismatic Li-ion cells. The arrangement used in this thesis includes additional thermocouples near the middle of the cell surface and near the terminals, as strong temperature gradients are anticipated in these areas. Additional thermocouples are also added to the perimeter of the cell to allow interpolation of the temperature distribution across the entire cell surface.

Charging and discharging are controlled by a battery test station from Greenlight Innovation (G12-200). Control and measurement accuracies for the test station are given in Table 3.1.

Characterization of cell discharge performance and thermal behaviour is conducted under two distinct heat transfer scenarios. The first promotes the formation of temperature gradients by sheathing the cell inside an insulated case, and the second minimizes temperature gradients by

submerging the cell in a circulating liquid bath with high heat capacity. Both scenarios are described in detail in the following subsections.
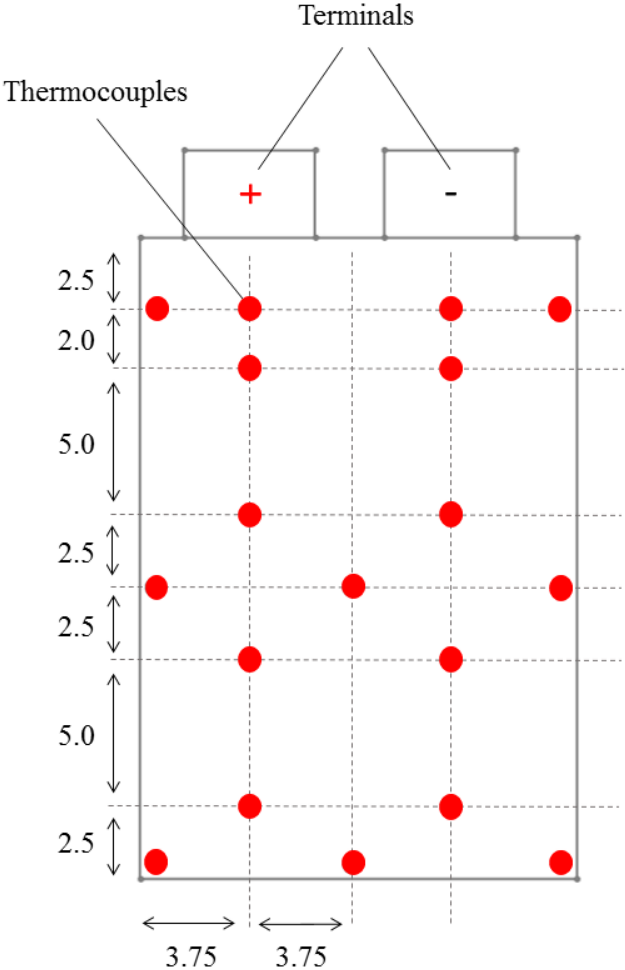
Figure 3.1: Thermocouple arrangement on Li-ion cell surface. All measurements are in cm.

Table 3.1: G12-200 battery test station accuracy.

Parameter	Accuracy
Current source control	$\pm$ 0.2A
Current sink control	$\pm$ 0.03A
Current measurement	$\pm$ 0.06A
Voltage source control	$\pm$ 0.05V

3.1   Cell Testing Setup 1

As pictured in Figure 3.2, the cell is surrounded on all sides (total surface area, including terminals, of 831 cm^2) by 5 cm thick of fiberglass insulation with a thermal resistance of 2.11 K·m^2/W, and then placed in an aluminum case with a thermal conductivity of 205 W/m·K. The fiberglass insulation layer serves two purposes: to inhibit the local dissipation of heat from the cell surface, reinforcing the formation of temperature gradients and clearly highlighting regions of higher-than-average and lower-than-average heat generation; and to create an immediate environment around the cell with known heat-transfer properties. The aluminum case serves to contain the insulation layer and provide a quiescent environment while rapidly conducting heat from the exterior of the insulation layer to the ambient. Two holes in the terminal end of the case allow the cell terminals and mounted thermocouples to be connected to the battery test station. The cell is supported at all four corners by PC-ABS plastic stands to avoid compressing the insulation underneath the cell.

To control the ambient temperature, the insulated cell assembly is placed inside an air convection temperature chamber (Cincinnati Sub-Zero MC-3, ±0.5^{o}C). Discharge is performed at -10°C and charging at 20°C.
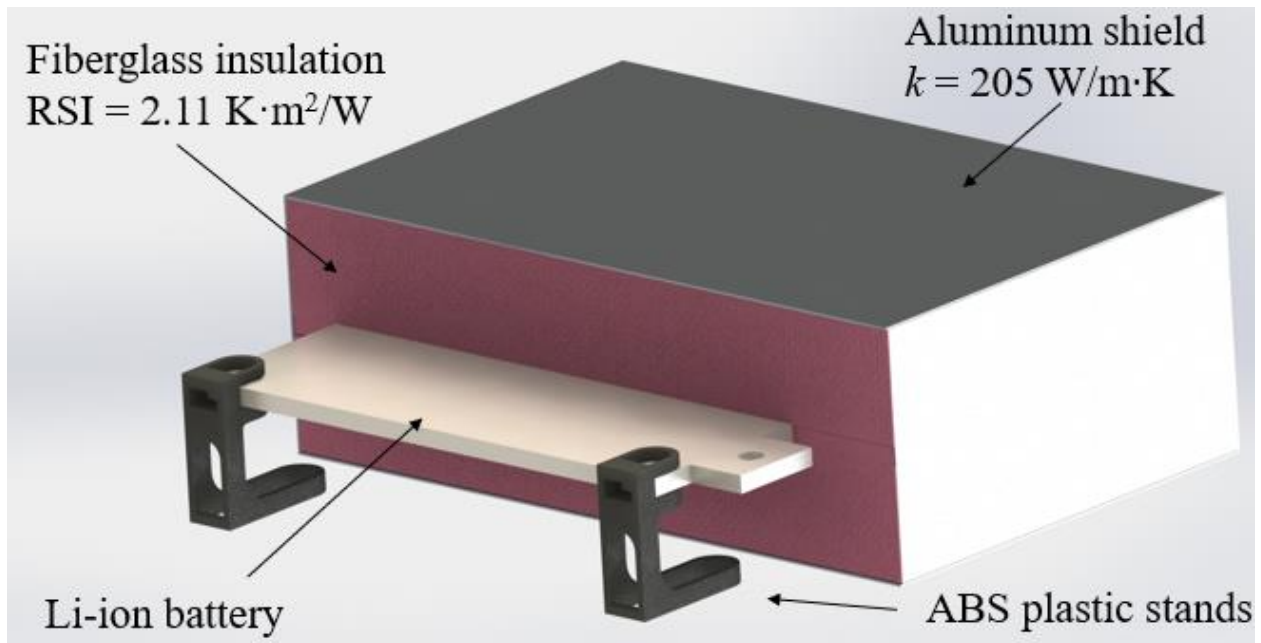
Figure 3.2: Isometric section view of insulated cell assembly.

3.2 Cell Testing Setup 2

To achieve an experimental approximation of thermally uniform discharge, this thesis uses the water/ethylene glycol bath method of temperature control developed by Chen and Li [29]. The cell is submerged in a forced convection thermal bath (ThermoFisher Haake AC200, $\pm0.1^\circ$C). The cell body, excluding the terminals, is immersed in a 50/50 water/ethylene glycol solution and fitted with an insulating cover ($22.5\times24.5\times2.5$cm) with a thermal resistance of 0.87 K·m^2/W. The cell terminals are exposed above the cover and connected to the battery test station. Discharge is performed at a variety of temperatures between -10 – 12°C for the purposes of model validation (see Table 3.2 for specific temperatures tested). At temperatures below -10°C, the cells are observed to reach the lower cutoff voltage of 2.6V too rapidly to allow for meaningful temperature gradients to develop, and therefore -10°C is selected as the lower limit temperature for the purposes of this thesis. Charging is performed at 20°C.

The entire experimental setup, including thermal bath, environmental chamber, and battery test station, is illustrated in Figure 3.3.

Table 3.2: Ambient temperature maintained during discharge. All tests in the environmental chamber are performed at -10°C, whereas the temperature of thermal bath depends on discharge rate as discussed in Section 5.1.

	Discharge rate	Ambient Temperature(s) (^{o}C)
Environmental Chamber	2C, 2.5C, 3C	-10
Thermal Bath	2C	-10, 0, 7
	2.5C	-10, 1.8, 10
	3C	-10, 2.6, 12
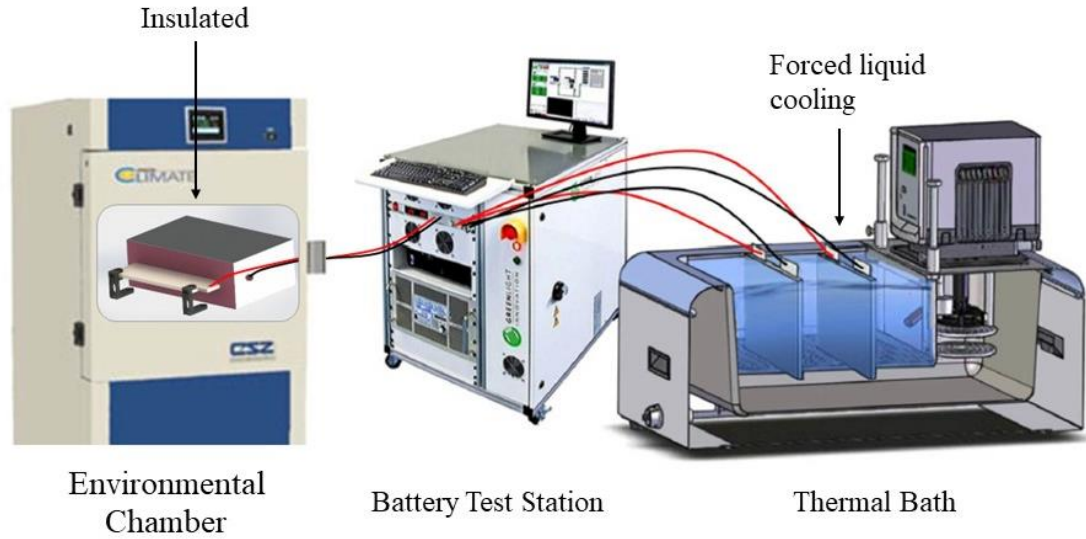
Figure 3.3: Experimental setup consisting of environmental chamber with insulated cell, battery test station, and thermal bath.

3.3   Cell Cycling

To facilitate comparison between the results of this and other studies, charge and discharge rates are reported as non-dimensionalized C-rates which are normalized to the cell's rated capacity. 1C discharge corresponds to the rate at which 100% of the cell's rated capacity will be depleted in one hour under nominal conditions (in the case of a 19.5Ah cell, 1C is 19.5A); 2C is twice the rate of 1C discharge; etc.

All discharge tests begin with a fully charged cell. A constant current is drawn from the cell at one of three rates (2C, 2.5C, 3C) at a given ambient temperature (see Table 3.2) until a lower cutoff voltage of 2.6V is reached. Tests are performed in semi-random order such that no two subsequent tests have the same set of rate and temperature conditions.

The upper and lower discharge rates of 2C and 3C, respectively, are selected for two reasons: 1) numerical investigations of EV energy consumption suggest that highway driving predominantly involves discharge rates between 2C – 3C [31]; and 2) lower and higher discharge rates do not produce meaningful temperature gradients for the purposes of this study.

Following discharge, the ambient temperature is brought to 20°C by the environmental chamber or thermal bath, and the cell is allowed to equilibrate to this temperature for four hours [2] before being charged at C/4. Charging follows the standard constant current, constant voltage (CCCV) method and ends at an upper cutoff voltage of 3.65V. The cell is then brought to the next discharge temperature for four hours before the next discharge commences. This cycling profile is plotted in Figure 3.4.

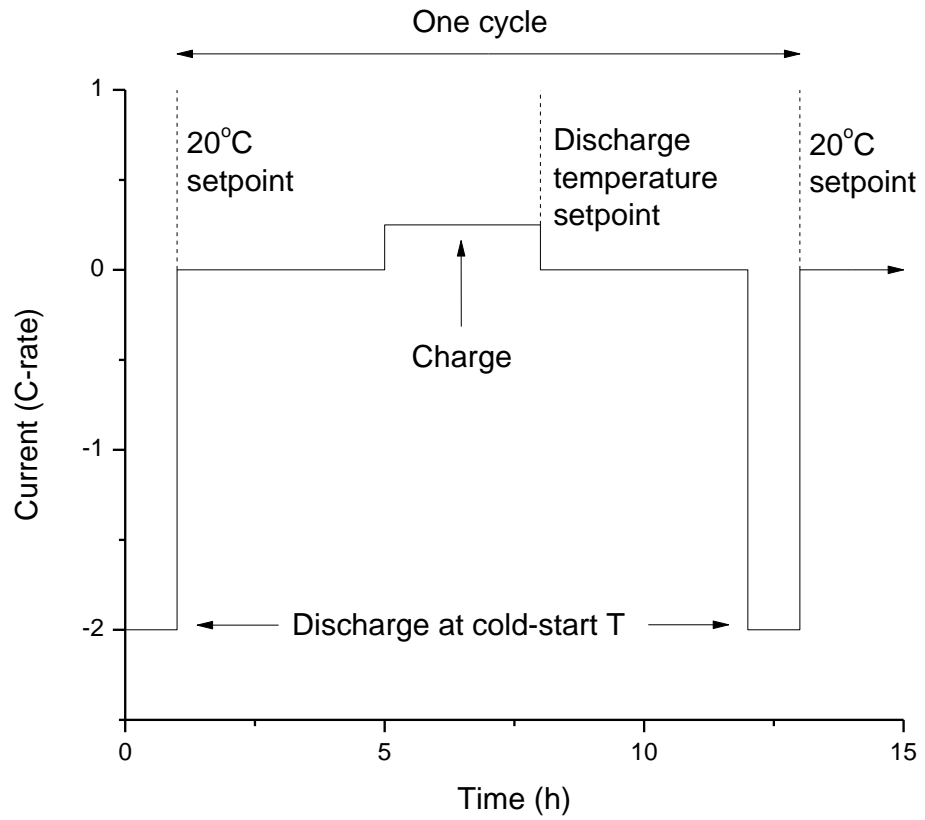Figure 3.4: Cycling profile for cell testing at various discharge rates and ambient temperature setpoints. For illustrative purposes, a discharge rate of 2C is shown.

4 Coupled Electrochemical-Thermal Model

In the present study, an electrochemical-thermal model of a Li-ion cell, developed by EC Power [49] and distributed as the software product AutoLion, is validated and then used to investigate the effects of spatial thermal non-uniformities on cell performance under otherwise identical operating conditions. The model is largely premised on the work of Gu and Wang [14] and simultaneously solves for a cell's transient thermal energy balance and various electrochemical and physicochemical properties in three dimensions in order to provide spatially-resolved values of such properties as temperature, current, potential, and SOC. Coupling between the thermal and electrochemical solutions accounts for the strong influence of temperature on electrochemical activity, and of electrochemical activity on heat generation.

4.1 Model Description

The model accounts for the following phenomena: Li particle intercalation and de-intercalation at the electrode-electrolyte interface; transport of charge in solid materials and electrolyte; transport of Li/Li$^+$ species; solid-phase Li diffusion in active materials; and thermal behaviours [49]. It makes the following assumptions: 1) no gas phase is present; 2) concentrated binary electrolyte is assumed; 3) side reactions are negligible (though an SEI layer resistance is assumed); 4) charge transfer kinetics are described by the Butler-Volmer equation; 5) ionic species transport in the electrolyte occurs only by diffusion and migration; 6) active material in the electrode is composed of spherical particles of uniform size; 7) volume change during cell operation is negligible; 8) electrode porosity is constant; 9) Li transport in active material particles occurs by diffusion with a constant diffusion coefficient D_s; 10) interfacial chemical equilibrium exists in the electrolyte phase due to high mass diffusivity; 11) interfacial chemical equilibrium exists in both electrolyte and solid phases due to high electronic conductivity and small radius of active material particles, respectively [49, 50].

The electrochemical component of the model considers the cell as composed of the two electrodes plus current collectors, the separator, and the electrolyte, as represented in Figure 4.1.
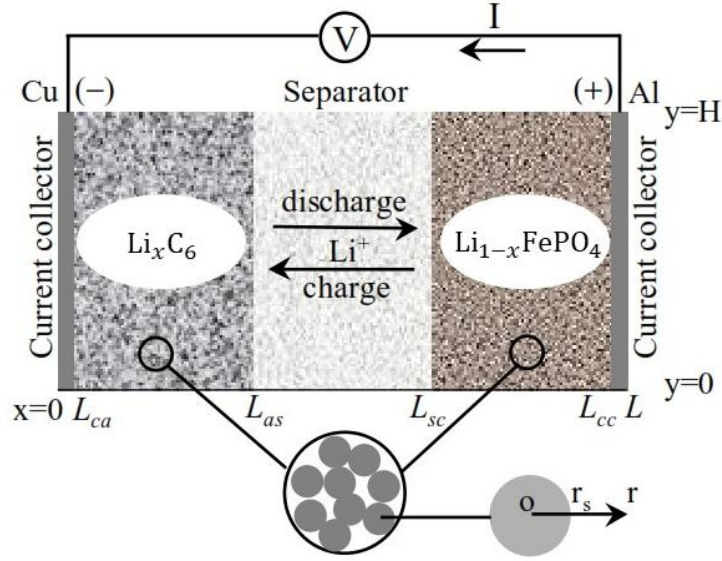
Figure 4.1: Schematic of model Li-ion cell showing current collectors, electrodes with spherical active material particles of radial geometry, and separator. Modified from [50].

Electrode kinetics are described by the Butler-Volmer equation, which governs the reaction rate at each electrode:

$$\bar{\iota}_{nj} = i_{oj} \left[\exp\left(\frac{\alpha_{aj}F}{RT}\eta_j\right) - \exp\left(-\frac{\alpha_{cj}F}{RT}\eta_j\right) \right] \tag{4.1}$$

where $\bar{\iota}_{nj}$ (A/cm^2) is the transfer current density, i_{oj} (A/cm^2) is the exchange or equilibrium current density when no net current is applied across the cell, α_{aj} and α_{cj} are the charge transfer coefficients at the anode and cathode, respectively, and η_j (V) is the surface overpotential on the electrodes. The equation relates cell current discharge to the equilibrium current, the reaction rates at the electrodes, and the cell overpotential or total internal resistance. Overpotential is expressed as,

$$\eta_j = \phi_s - \phi_e - U_j - \bar{\iota}_{nj}R_f \tag{4.2}$$

where ϕ_s and ϕ_e (V) are the electric potential of the solid and electrolyte phases, respectively, U_j (V) is the open-circuit potential when no net current is applied and is itself a function of temperature and SOC, and R_f (Ω/m^2) is the SEI layer resistance.

31

The model assumes the only reactions occurring in the cell are the oxidation and reduction of lithium at the electrodes, and that no side reactions occur.

Conservation of lithium in the solid and electrolyte phases assumes that transport is by diffusion only; that electrolyte diffusivity is very high such that lithium concentration at the solid-electrolyte interface is equal to that in the bulk electrolyte; that the cell has a constant porosity with no volume change; and that the electrodes are composed of uniform spherical particles clustered into agglomerates. The model holds that the rate of diffusion through an agglomerate is much slower that the rate of diffusion through the pore spaces between agglomerate clusters, and therefore diffusion within the agglomerate clusters dominates diffusion in the electrode, and diffusion in the pore spaces is neglected.

Conservation of Li$^+$ in the electrolyte phase is expressed as,

$$\frac{\partial}{\partial t}[\varepsilon C_e] = \nabla \cdot \left(D_e^{\text{eff}} \nabla C_e\right) + \frac{1 - t_+^0}{F} j^{\text{Li}} \tag{4.3}$$

where ε is porosity expressed as a volume fraction, C_e (mol/cm^3) is Li$^+$ concentration, t_+^0 is the transference number of Li$^+$, j^{Li} (A/cm^3) is the reaction current to produce/consume Li/Li$^+$, and D_e^{eff} (cm^2/s) is the effective diffusion coefficient in the electrolyte, corrected for the effect of porosity and expressed by the Bruggeman relationship:

$$D_e^{eff} = D_e \varepsilon \tag{4.4}$$

where D_e is the electrolyte-phase diffusion coefficient.

Equation 4.3 describes the change in Li$^+$ concentration in the electrolyte as a result of transport by diffusion due to concentration gradients and the electrical field effect between two electrodes of different potentials, as well as a source term in the form of the reaction current that drives lithium oxidation and reduction. It assumes a constant transference number and neglects any transference gradient.

Conservation of active material Li species in the solid phase assumes a representative active material particle of spherical geometry and thus is discretized in the radial direction. The spherical geometry is consistent with the porous electrode theory and uniformly-sized spherical

active material particles assumed by Doyle et al. [11, 40] and carried forward in subsequent models [2, 11, 12, 14, 34, 44, 51]. Li species material conservation in solid phase is expressed as,

$$\frac{\partial C_s}{\partial t} = \frac{1}{r^2}\frac{\partial}{\partial r}\left(D_s r^2 \frac{\partial C_s}{\partial r}\right)$$ (4.5)

where C_s is the concentration of lithium in a particle, D_s is the diffusion coefficient of Li in the solid phase, and with boundary condition on particle surface:

$$-D_{s,i}\frac{\partial C_{s,i}}{\partial r}\bigg|_{r=R_i} = \frac{i}{F}$$ (4.6)

where i (A/cm^2) is the local current density on the particle surface. Similar to equation 4.3, equation 4.5 consists of a flux term, transport term, and source term.

Conservation of charge in the electrolyte assumes a concentrated binary electrolyte that enables the transfer of charge by ions undergoing diffusion, described by the electrochemical potential form of Ohm's law:

$$\nabla \cdot \left(k^{\text{eff}}\nabla\phi_e\right) + \nabla \cdot \left(k_D^{\text{eff}}\nabla \ln C_e\right) = -j^{\text{Li}}$$ (4.7)

where k^{eff} (S/cm) is the effective ionic conductivity of the electrolyte, corrected for the actual path length of species transfer through porous electrodes, and is determined by the Bruggeman relationship [52]:

$$k^{\text{eff}} = k\varepsilon \cdot k_D^{\text{eff}}$$ (4.8)

where k (S/cm) is the ionic conductivity. k_D^{eff} (A/cm) is the effective diffusional conductivity, and is defined as,

$$k_D^{\text{eff}} = \frac{2RTk^{\text{eff}}}{F}(t_+^0 - 1)\left(1 + \frac{d\ln f_+}{d\ln C_e}\right)$$ (4.9)

where $d\ln f_+ / d\ln C_e$ represents short range ion-solvent interactions and is negligible for dilute solutions (< 2.5 mol/L).

Equation 4.7 therefore describes charge transfer as made up of transport due to the electrical field effect of a potential gradient between electrodes as well as transport due to diffusion

along a concentration gradient, and a source term. The model assumes a stationary electrolyte, with no transport due to convection.

Conservation of charge in the solid phase, meanwhile, is driven by the flow of electrons along a potential gradient and is described simply by Ohm's law:

$$\nabla \cdot \left(\sigma^{\text{eff}} \nabla \phi_s\right) = j^{\text{Li}} \tag{4.10}$$

where σ^{eff} (S/cm) is the effective electrical conductivity of the porous solid electrode.

The model's thermal component, meanwhile, is premised on a thermal energy balance:

$$\frac{\partial \left(\rho c_p T\right)}{\partial t} + \nabla \cdot (\mathbf{v}T) = \nabla \cdot \lambda \nabla T + q \tag{4.11}$$

where ρ (g/cm^3) is volume-averaged density, c_p (J/kg·K) is volume-averaged specific heat, $\mathbf{v}$ (cm/s) is the velocity vector of the electrolyte, λ (W/cm·K) is volume-averaged thermal conductivity, and q (J/cm^3·s) is the volumetric heat generation rate. The LHS of the equation describes heat storage and convection, and the RHS describes conduction and generation. For cells with stationary electrolytes, including the LiFePO$_4$ cells used in this study, the convection term is neglected [53].

Heat generation q is expressed as,

$$q = A_e \int_0^L j^{\text{Li}} \left(T \frac{dU}{dT}\right) + j^{\text{Li}}\left(\phi_s - \phi_e - U_j\right) + \sigma^{eff} \nabla \phi_s \cdot \nabla \phi_s$$
$$+ k^{\text{eff}} \nabla \phi_e \cdot \nabla \phi_e + k_D^{\text{eff}} \nabla \ln C_e \cdot \nabla \phi_e dx \tag{4.12}$$

where A_e (cm^2) is the electrode area and L (cm) is the cell thickness excluding the current collectors. The first term on the RHS represents reversible heat due to entropy. The remaining terms on the RHS clearly illustrate the manner in which the above-described electrochemical processes are tightly coupled to heat generation and therefore to temperature, and represent heat generation due to charge transfer resistance, ohmic resistance, ionic conduction resistance, and concentration overpotential.

Heat transfer is solved in three dimensions by CFD software (ANSYS Fluent v15.0.7). Local cell temperature, in turn, influences a number of temperature-dependent physicochemical

parameters and phenomena identified in equations 4.1-4.10, such as diffusion coefficients, ionic conductivity, and exchange current density. The temperature-dependence of such parameters can be generally described by Arrhenius' equation:

$$\Phi = \Phi_{\text{ref}} \exp\left[\frac{E_{\text{act},\Phi}}{R}\left(\frac{1}{T_{\text{ref}}} - \frac{1}{T}\right)\right] \tag{4.13}$$

where Φ is the temperature-dependent physicochemical parameter, Φ_{ref} is the known value of that parameter at a given reference temperature, and $E_{act,\Phi}$ is the activation energy of the evolution process of Φ (the greater the activation energy, the more sensitive the parameter is to temperature). These modified parameters serve to couple the thermal model with a multiphase mass-transport and electrochemical kinetic model which solves for equations 4.1-4.10.

The model assumes uniform initial conditions, i.e.,

$$C_e = C_e^0, \ C_s = C_s^0 \text{ and } T = T^0 \tag{4.14}$$

No reaction occurs at the current collectors, giving the boundary conditions,

$$\frac{\partial C^{Li}}{\partial n} = 0 \text{ and } \frac{\partial \phi_e}{\partial n} = 0 \tag{4.15}$$

At the tops of the current collectors (i.e. the terminals), current is applied and heat dissipates, such that at y = H and x < L_{ca} or x > L_{cc} (refer to Figure 4.1),

$$-\sigma^{eff}\frac{\partial \phi_s}{\partial y} = I \text{ and } -\lambda\frac{\partial T}{\partial y} = \text{h}(T - T_a) \tag{4.16}$$

where I (A/cm^2) is the applied current density, λ (W/m·K) is thermal conductivity, h (W/cm^2·K) is the convective heat transfer coefficient, and T_a (K) is the ambient temperature.

At all other boundaries,

$$\frac{\partial \phi_s}{\partial n} = 0 \text{ and } -\lambda\frac{\partial T}{\partial n} = \text{h}(T - T_a) \tag{4.16}$$

Numerical solutions and material properties are provided in the commercial software package AutoLion, developed by EC Power [49].

The model discretizes the cell using a finite control volume approach with a three-grid mesh (see Figure 4.2). The thermal energy balance (equation 4.11) is solved on the macro-grid, conservation of charge (equations 4.7 and 4.10) and of electrolyte-phase Li^+ species (4.3) are solved on the meso-grid, and solid-state diffusion inside active material particles (4.5) are solved on the micro-grid. There is one representative active material particle within each electrode meso-grid control volume. The model can be converted to a 0D thermal model by removing discretization on the macro-grid and instead solving for a single global cell temperature.
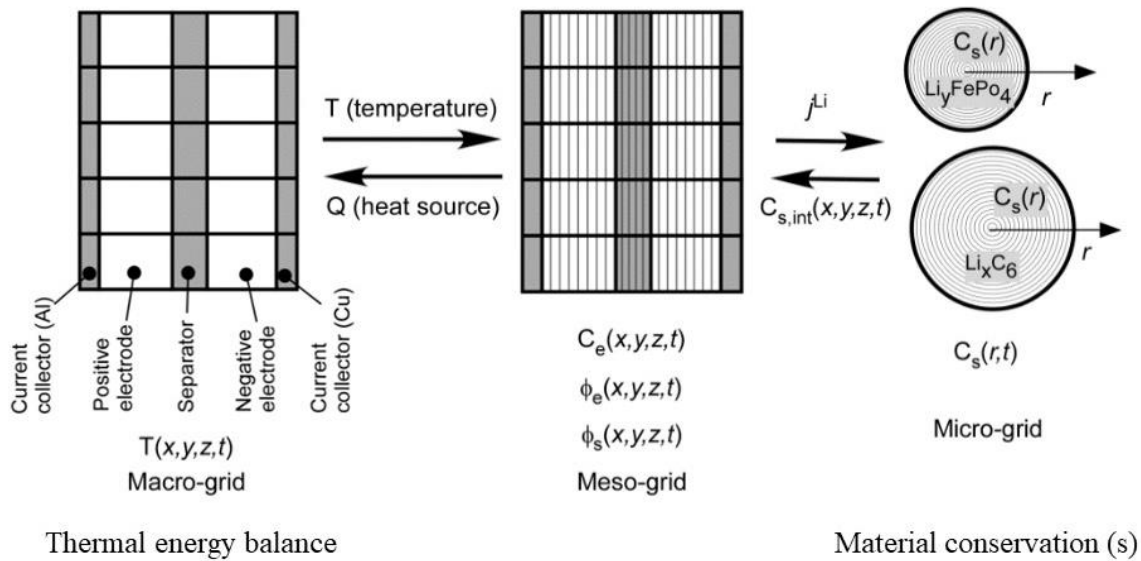
Figure 4.2: Schematic diagram of three-grid mesh utilized for model cell discretization. The simulation domain is divided into three domains: thermal macro-grid, electrochemical meso-grid, and spherical micro-grid for solid state diffusion. Modified from [49].

4.2 Three-Dimensional Model Setup

The 3D electrochemical-thermal coupled model employed for this study is provided by the AutoLion software package version 3.2.4 [49]. Material property values for a prismatic LiFePO$_4$ cell are provided within the software. A full list of model cell design parameters is provided in Section 8 (Appendix I).

The cell type is a stacked electrode design (SED) with dimensions 160x227x7.25mm, and reversible capacity of 19,500 mAh per the manufacturer's specifications. The upper and lower

cutoff voltage are 3.65 and 2.6 V, respectively, and open circuit voltage (OCV) at 100% state of charge (SOC) is 3.55 V. Simulations were run at 2C, 2.5C, and 3C discharge. All simulations were set to initial conditions of 100% SOC and a uniform cell temperature of 263.15 K. Boundary conditions were set at 263.15 K and a heat transfer coefficient of $h = 0.47$ Wm^{-2}K^{-1} to match experimental conditions. A full list of simulation parameters, including cell mesh construction, is provided in Section 9 (Appendix II).

4.3   Lumped Thermal Model Setup

The cell design parameters described in Section 4.1 and parameterized in Sections 8 and 9 were also carried for the 0D lumped capacitance model. Simulations were carried out under 0D heat transfer conditions using a lumped thermal model by building a cell "pack" of a single cell within the simulation parameters. All simulations were set to initial conditions of 100% SOC and a uniform cell temperature of 263.15 K. Simulations carried identical boundary conditions as assigned to the 3D model to represent the behaviour of a thermally uniform cell. Simulations were also carried out under constant-temperature conditions at various near- and sub-zero temperatures where cell temperature was not permitted to change, to allow validation of cell behaviour when temperature rise is negligible.

5 Results and Discussion

In this study, a thermally coupled electrochemical model is validated and then used to evaluate the effects of temperature distributions on Li-ion cell performance at low temperatures. First, an experimental characterization of electrical and thermal behaviour is performed under different heat transfer conditions at near- and sub-zero temperatures. Next, model agreement with these experimental results is examined. Finally, a series of simulations is employed to investigate the effects of thermal non-uniformity on cell capacity and voltage behaviour.

5.1 Experimental Characterization of Low-Temperature Discharge

Characterization of LiFePO$_4$ cells is performed according to the methods described in Section 3. All results presented in this section represent the average measurements of three separate, identical tests for three cells each, for a total of nine repeated tests. The standard error of voltage and temperature measurements for each set of repeated tests is well within the bounds of voltage measurement accuracy ($\pm$ 0.05 V) and thermocouple accuracy ($\pm$ 0.5 ^{o}C), indicating good repeatability of the obtained results.

The mean temperature rise of an insulated cell (h = 0.47 Wm^{-2}K^{-1}, see Section 3.1) operating at an initial temperature of -10 ^{o}C is illustrated in Figure 5.1 for 2C, 2.5C, and 3C discharge. Mean temperature rise is calculated as the arithmetic mean of temperature rise at the measured thermocouple locations.

Figure 5.1 shows that mean cell temperature increases during the course of discharge, reaching a maximum at the end of discharge. The rate of temperature rise changes, however, over the course of discharge, corresponding to changes in the magnitude of three fundamental internal resistances: charge transfer resistance, ohmic resistance, and mass transport resistance. Temperature rise is most rapid at the onset (energy discharged < 6 Ah) and end (> 13 Ah) of discharge, corresponding to high charge transfer resistance and high cathode-side mass transport resistance, respectively. At the cell's initial low temperature, charge transfer kinetics are sluggish, generating internal resistance, and as discharge nears completion, the high concentration of lithium

38

at the cathode impedes further intercalation, resulting in mass transport resistance. Between 6 Ah and 13 Ah of discharge, ohmic resistance dominates, and temperature rise is approximately linear. Discharge rate also has a clear effect on temperature rise, with higher C-rates resulting in greater cell impedance and therefore greater temperature rise. The total temperature rise at each discharge rate is given in Table 5.1.
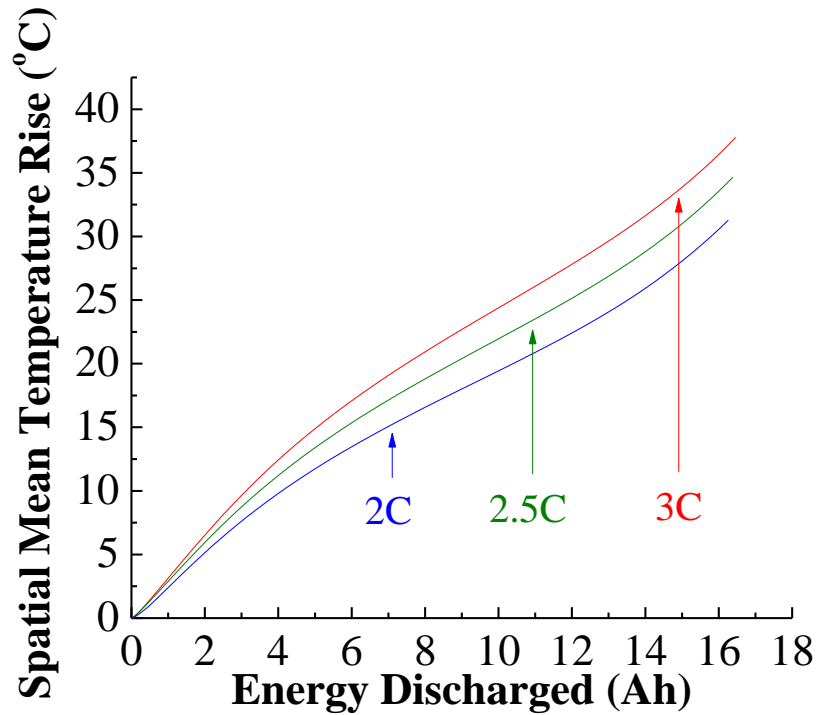

Figure 5.1: Mean temperature rise of an insulated cell operating at an initial temperature of -10°C for 2C, 2.5C, and 3C discharge.

Table 5.1: Maximum mean temperature and temperature rise at the end of discharge for an insulated cell at an initial temperature of -10°C.

Discharge Rate	Maximum Mean Temperature (°C)	Mean Temperature Rise (°C)
2C	21.3	31.3
2.5C	24.6	34.6
3C	27.8	37.8

Cell voltage behaviour is plotted in Figure 5.2 for the same set of insulated cell conditions above. Voltage drop is significant at the onset of discharge due to high impedance, and high charge transfer resistance in particular, and reaches as low as 2.74 V at 3C discharge. As discharge proceeds, heat generation within the cell lessens impedance, which in turn enables higher operating voltage, and voltage recovery is observed. It can be seen that very similar discharge capacity is achieved regardless of discharge rate, demonstrating the feedback relationship between electrochemical and thermal behaviour. Cell impedance, and therefore temperature rise, is proportional to discharge rate. As discharge rate increases, additional irreversible heat is generated, reducing impedance and encouraging voltage recovery. This self-heating tendency of cells operating at low temperatures thus creates a negative feedback loop wherein cell impedance is diminished over the course of discharge, countering the otherwise high impedance caused by rapid discharge.
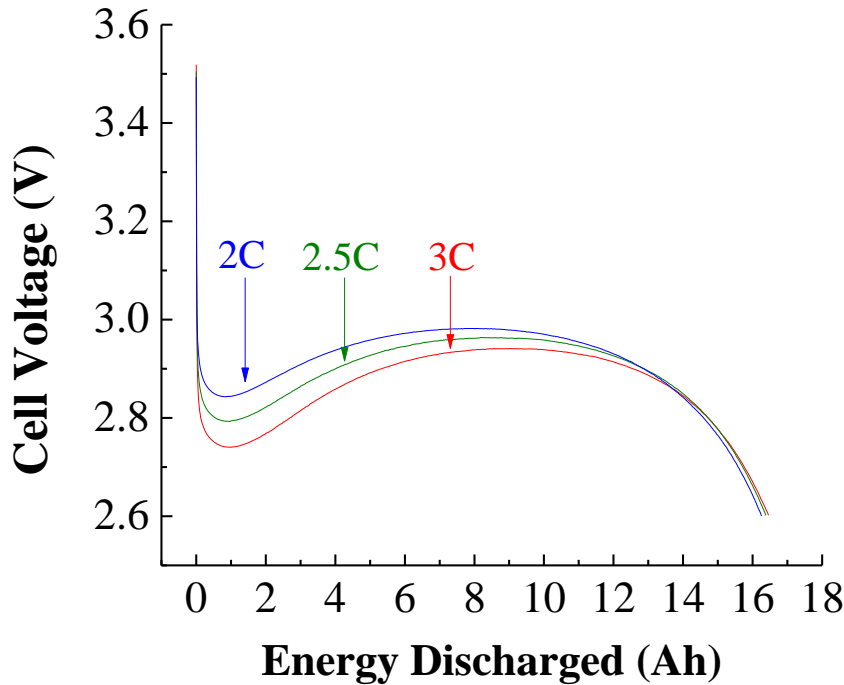
Figure 5.2: Discharge voltage behaviour of an insulated cell operating at an initial temperature of -10 °C for 2C, 2.5C, and 3C discharge.

Spatial thermal behaviour is illustrated in Figure 5.3, which shows temperature distributions formed under insulated cell conditions at an initial temperature of -10°C. These distributions are obtained at the end of discharge, when temperature non-uniformity is greatest. Local temperature rise is estimated by plotting temperature rise at each of the 18 thermocouple locations, and interpolating those values across a 76×101 node grid. Linear interpolation is used. Detailed information on the MATLAB function used to generate these plots is available through Mathworks [54]. The temperature distributions plotted in Figure 5.3 are therefore approximations only; temperature is known only at the 18 thermocouple locations, and only these known values are used in model validation. However, for descriptive purposes, these plots aid in the visualization of local temperature patterns, and the known temperature values at each thermocouple are indicated. It is observed that at 2C discharge, temperature rise is greatest near the centre of the cell and towards the positive terminal. As discharge rate increases, temperature rise at the positive terminal becomes increasingly dominant, with strong gradients forming in that region during 3C

discharge. This observation is consistent with previous studies of the thermal behaviour of prismatic Li-ion cells, and can be attributed to local current density. The edge current collection design of these cells results in high local current density near the terminals which increases with discharge rate. The positive terminal in particular undergoes significant temperature rise because the terminal's aluminum current collector plate has greater electrical resistivity than the negative terminal's copper plate, resulting in substantial Joule heating near the positive terminal. It can also be seen that the magnitude of local temperature variations increases with discharge rate. Local maxima and minima in temperature rise at the end of discharge are given in Table 5.2 for each discharge rate.
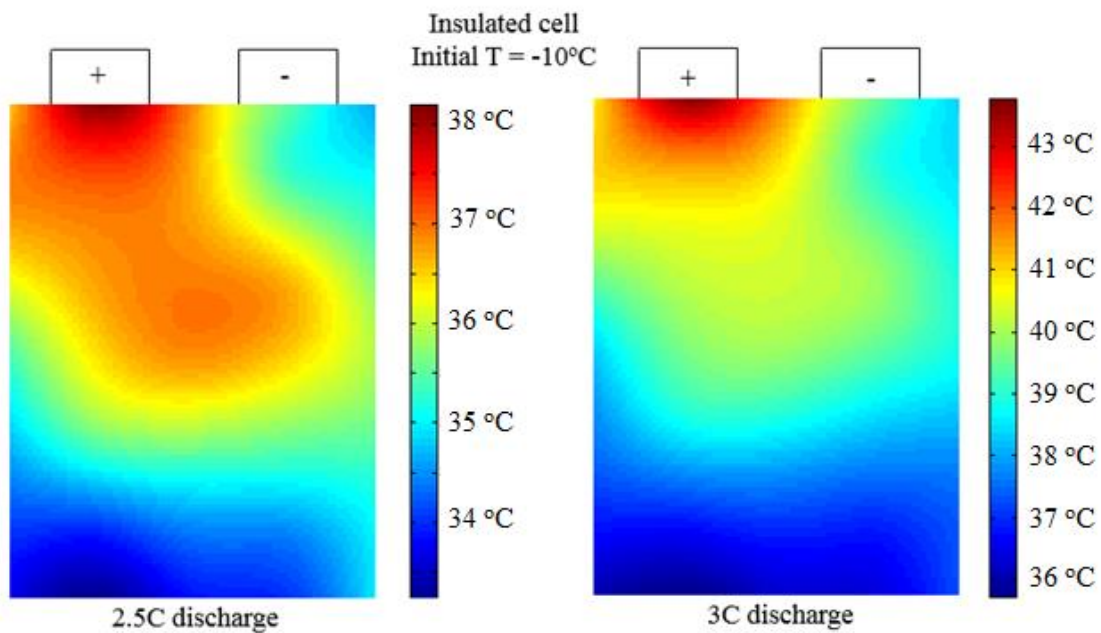

Figure 5.3: Temperature distributions formed under insulated cell conditions at an initial temperature of -10 $^{\circ}$C, as measured at the end of discharge.

Table 5.2: Minimum and maximum local temperature rise, and maximum difference in local temperature, at the end of discharge for an insulated cell at an initial temperature of 10 ^{o}C.

Discharge Rate	Minimum Local Temperature Rise (^{o}C)	Maximum Local Temperature Rise (^{o}C)	Maximum Spatial Temperature Difference (^{o}C)
2C	30.5	33.4	2.9
2.5C	33.7	38.0	4.3
3C	36.1	43.3	7.2

This dependence of thermal non-uniformity on discharge rate is further illustrated in Figure 5.4 and Figure 5.5. In Figure 5.4, temperature rise at each thermocouple is plotted against energy discharged for 2C, 2.5C, and 3C discharge, respectively. The increase in both absolute cell temperature and in temperature variation with discharge rate is clearly evident. These results are summarized in Figure 5.5, which plots the standard deviations of temperature rise across all 18 thermocouple locations against energy discharged for the same discharge rates. The standard deviation values reflect the magnitude of thermal non-uniformity, with greater standard deviation signifying greater local temperature deviations from the spatial mean. It is evident in Figure 5.4 and Figure 5.5 that as discharge progresses, thermal non-uniformity increases, with higher discharge rates producing greater non-uniformity.

The above characterization represents thermal and voltage behaviour for a cell exhibiting a non-uniform temperature distribution, under conditions that promote temperature rise. Next, characterization is performed for a cell exhibiting nearly uniform thermal behaviour, under conditions that inhibit temperature rise, using a temperature-controlled thermal bath (see Section 3.2).
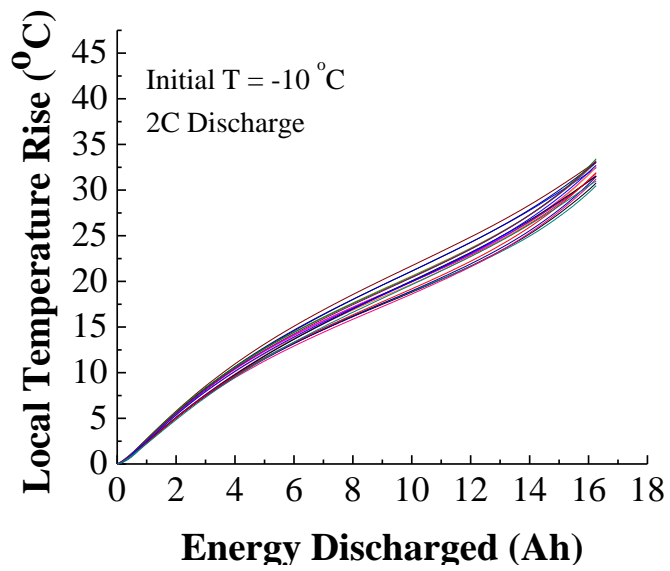
(a) 2C discharge
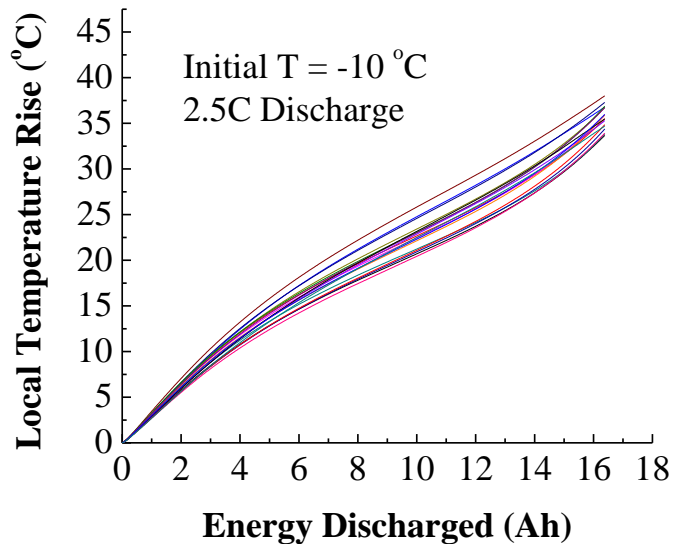
(b) 2.5C discharge
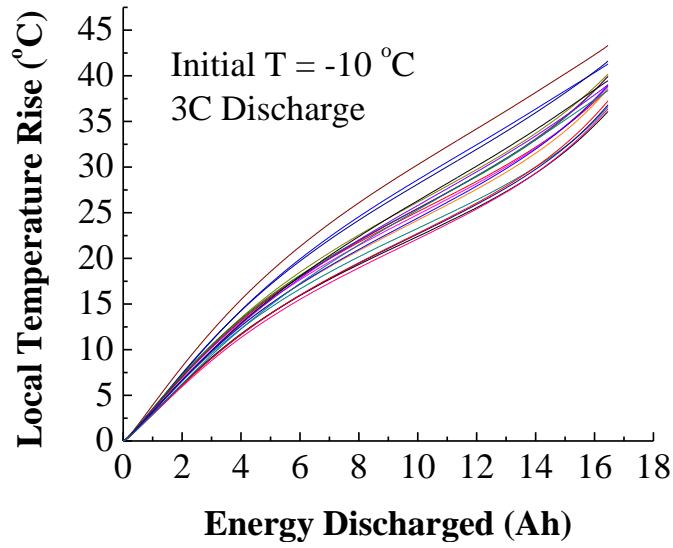
(c) 3C discharge

Figure 5.4: Temperature rise at each thermocouple against energy discharged for (a) 2C, (b) 2.5C, and (c) 3C discharge.

Figure 5.5: Standard deviation of local cell temperature rise at 18 thermocouple locations during 2C, 2.5C, and 3C discharge.

Whereas temporal variations in temperature were large under insulated cell conditions, such variations are minimal under thermal bath conditions, and so to obtain characterization results across a meaningful temperature range, multiple ambient temperatures are used. Appropriate ambient temperatures were determined 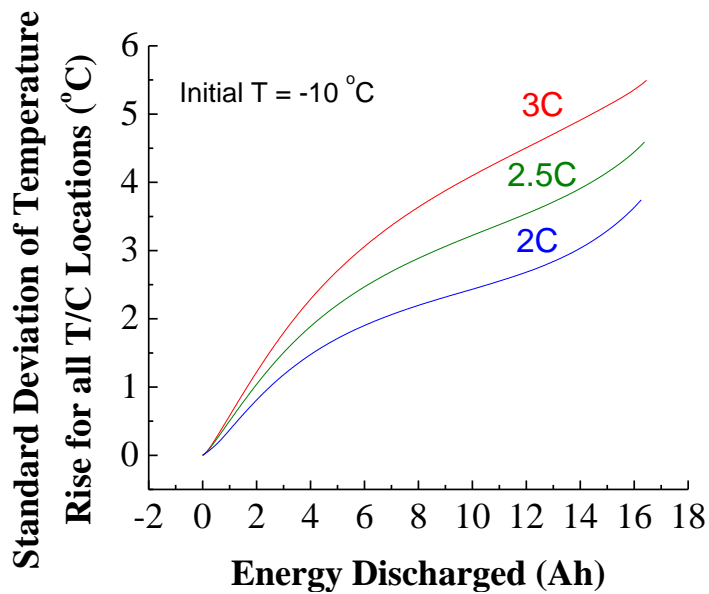by first discharging a cell at an initial temperature of -10°C in a quiescent environment at an ambient temperature of -10°C and with natural air convection as the dominant mechanism of heat transfer in order to observe mean temperature rise. This procedure was repeated for 2C, 2.5C, and 3C discharge. Next, thermal bath setpoint values were chosen as the minimum and maximum mean temperature rise for each discharge rate. Finally, cell temperature was averaged, both spatially and temporally, for the entire duration of discharge to provide a spatial-temporal mean temperature value for each discharge rate. This value represents the overall average operating temperature for a cell discharging at a given rate under natural air convection conditions, and is used as an additional setpoint temperature for testing under thermal bath conditions. These three setpoint values and their relation to temperature rise under natural convection are illustrated for 3C discharge in Figure 5.6. By using these three setpoint values for each discharge rate, cell behaviour can be observed across a meaningful range of temperature conditions that the cell might realistically be exposed to during normal sub-zero operation. Because temperature rise is dependent on discharge rate, a different set of three bath setpoint values is obtained for each discharge rate. These temperatures are given in Table 5.3.

The above-described bath temperatures were chosen to achieve cell characterization over a realistic operating temperature range, and thereby to enable model validation at various temperatures representative of cold-start conditions. Furthermore, characterization at the spatial-temporal mean temperature allows for comparison of cell performance under identical average temperature conditions but differing spatial temperature conditions: in one case, the spatial non-uniformity and temperature rise representative of cold-start operation and natural convection; and in the other case, the spatial uniformity and constant temperature representative of effective thermal management. Comparisons are made for 2C and 3C discharge in Figure 5.7. Note that under natural convection conditions, voltage recovery supports a higher discharge capacity than under nearly constant mean-temperature conditions. This can be attributed at least in part to the nonlinear relationship between temperature and internal resistance at subzero temperatures; as temperature decreases, internal resistance increases exponentially and heat generation correspondingly increases.
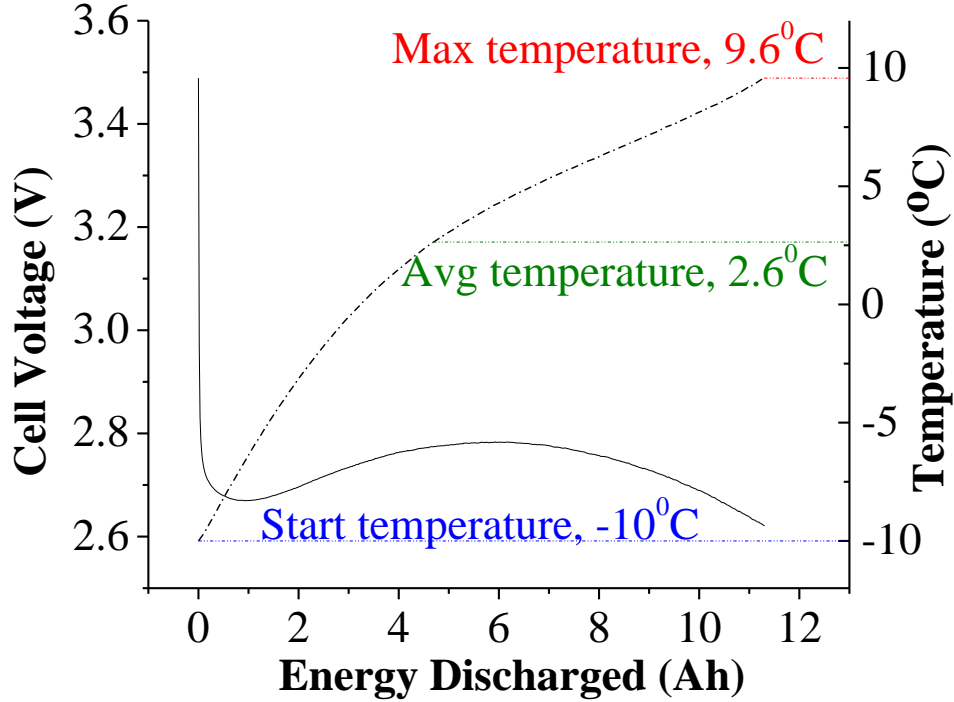
Figure 5.6: The method used to select thermal bath setpoint values is exemplified for 3C discharge. First, the cell is discharged under natural convection conditions at an ambient temperature of -10 °C in order to obtain a spatially-averaged temperature profile. Second, minimum and maximum setpoint values are selected based on the minimum and maximum values of the temperature profile (-10°C and 9.6°C). Third, the arithmetic mean of all points along the temperature profile is taken in order to obtain the spatial-temporal mean (2.6°C). This spatial-temporal mean is selected as the third setpoint value for 3C discharge tests in the thermal bath.

Table 5.3: Thermal bath setpoint values.

Discharge Rate	Setpoint 1 (ºC)	Setpoint 2 (ºC)	Setpoint 3 (ºC)
2C	-10	-0.1	7
2.5C	-10	1.8	10
3C	-10	2.6	12
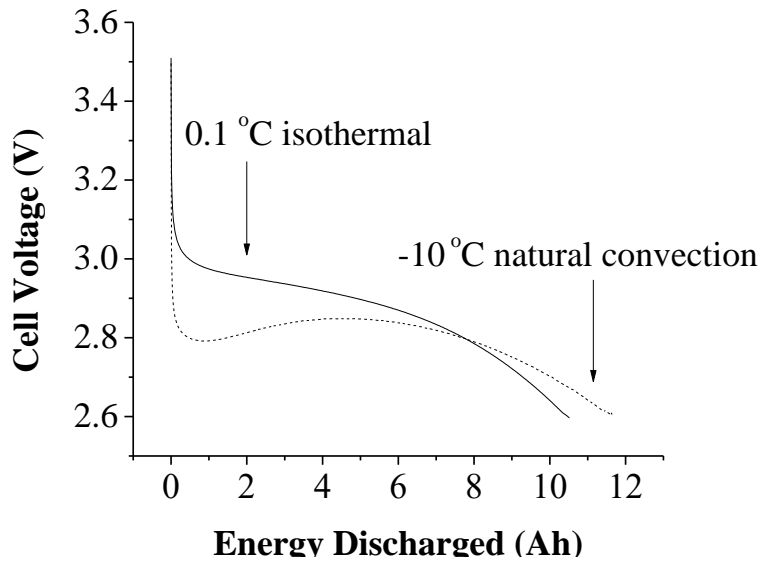
(a) 2C discharge
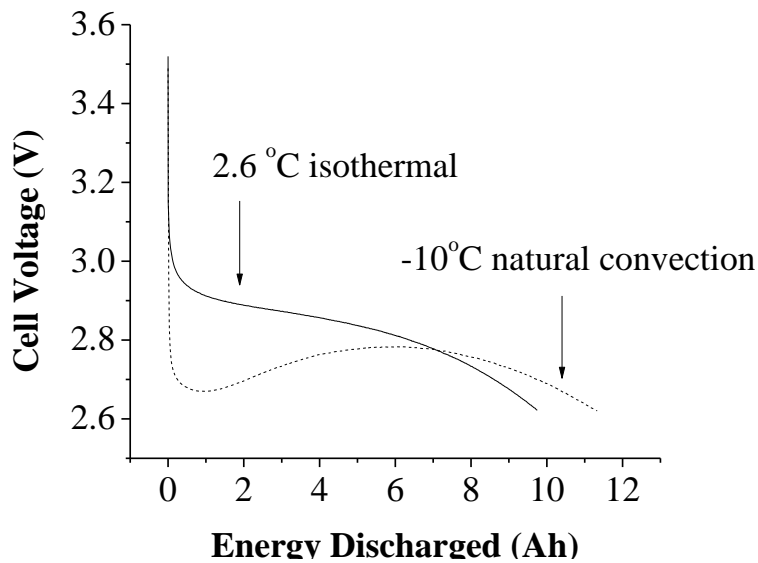
(b) 3C Discharge

Figure 5.7: Discharge voltage under natural convection, and the corresponding spatial-temporal mean under nearly isothermal conditions, shown for (a) 2C and (b) 3C discharge. The dotted line represents natural convection in the environmental chamber at -10 °C, while the solid line represents nearly isothermal conditions at the spatial-temporal mean temperature recorded for the preceding natural convection discharge.

Representative thermal characterization results are shown in Figure 5.8 and Table 5.4. Figure 5.8 compares the change in average cell temperature temporally over the course of discharge between the thermal bath conditions and the insulated cell conditions. It can be seen that for the thermal bath conditions, the average cell temperature is nearly constant throughout discharge. Maximum mean temperature rise is observed to be 1.8^{o}C, corresponding to 2.5C discharge. Table 5.4, meanwhile, illustrates the extent of spatial thermal uniformity for a cell under thermal bath conditions by plotting the local minima and maxima, as well as the standard deviation, of temperature rise across all thermocouple locations. It is observed that a cell in the thermal bath remains nearly thermally uniform, with a standard deviation across thermocouple locations of 0.2 – 0.3 ^{o}C, which is within the bounds of thermocouple accuracy ($\pm$ 0.5 ^{o}C). For the purposes of this study, therefore, characterization results obtained using thermal bath conditions are considered representative of an isothermal cell discharged at a constant temperature.
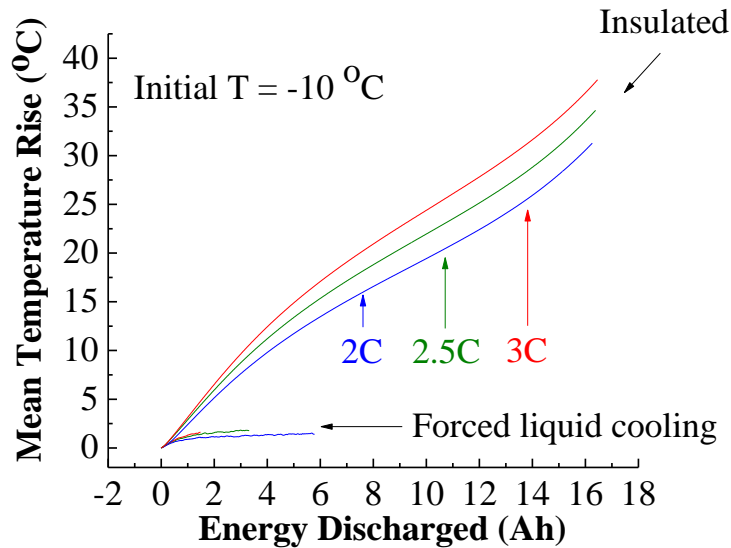
Figure 5.8: Mean cell temperature rise under thermal bath conditions as compared to insulated conditions.

Table 5.4: Local temperature rise and standard deviation across all thermocouple locations at the end of discharge for a cell operating under thermal bath conditions at a setpoint of -10°C.

Discharge Rate	Minimum Local Temperature Rise (ºC)	Maximum Local Temperature Rise (ºC)	Standard Deviation Across All T/C Locations (ºC)
2C	1.2	1.7	0.2
2.5C	1.4	2.4	0.3
3C	1.3	1.9	0.2

5.2 Model Validation

In this subsection, the characterization data described above are used to validate two models of cell thermal and electrical behaviour: a one-dimensional isothermal model and a fully three-dimensional model.

5.2.1 0D Model Validation

Characterization data obtained under thermal bath conditions as described above in Section 5.1 are used to validate a 0D lumped capacitance thermal model. Model setup and parameterization are described above in Section 4.2. Simulations are performed under isothermal, constant-temperature conditions, with temperature held at the same setpoints as those used for experimental characterization and summarized in Table 5.3. Validated voltage curves are shown below in Figure 5.9.
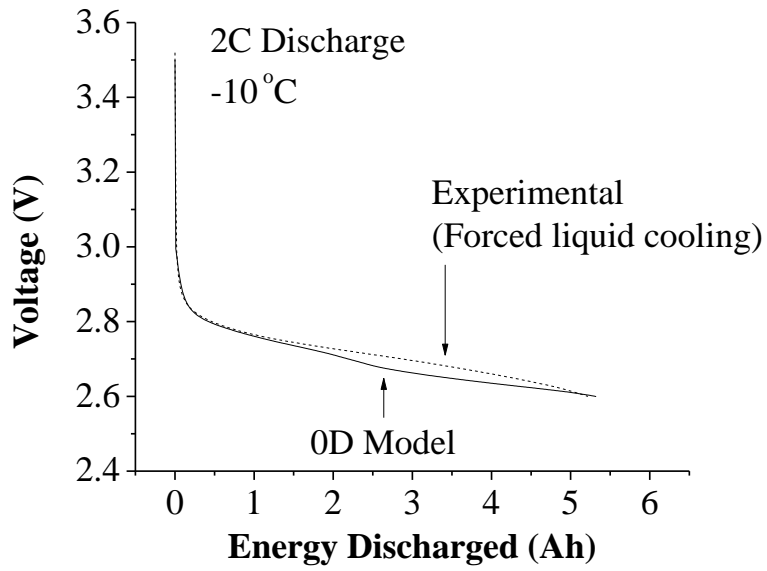
(a)
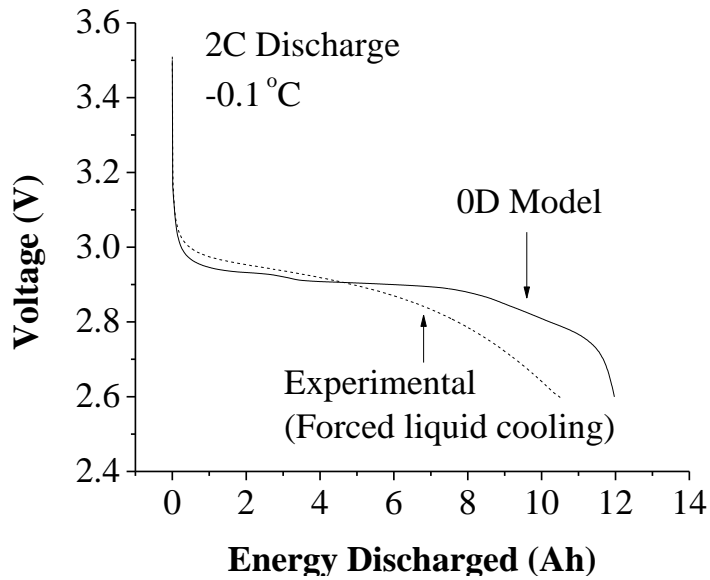
(b)
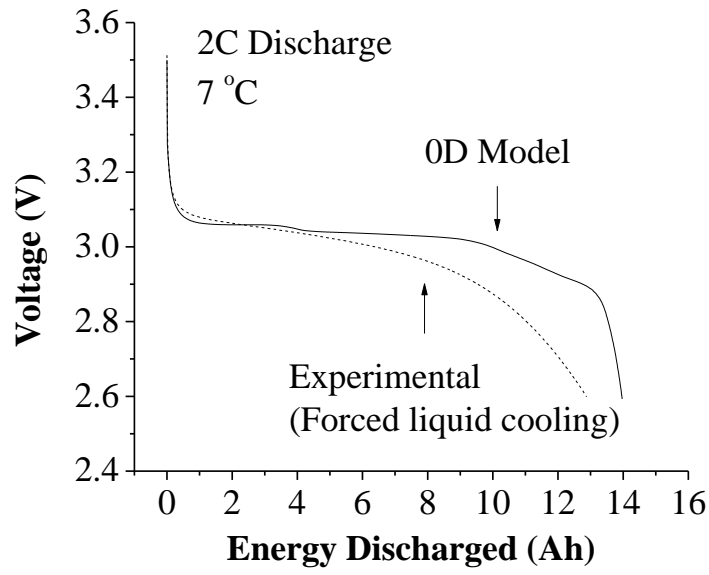
(c)
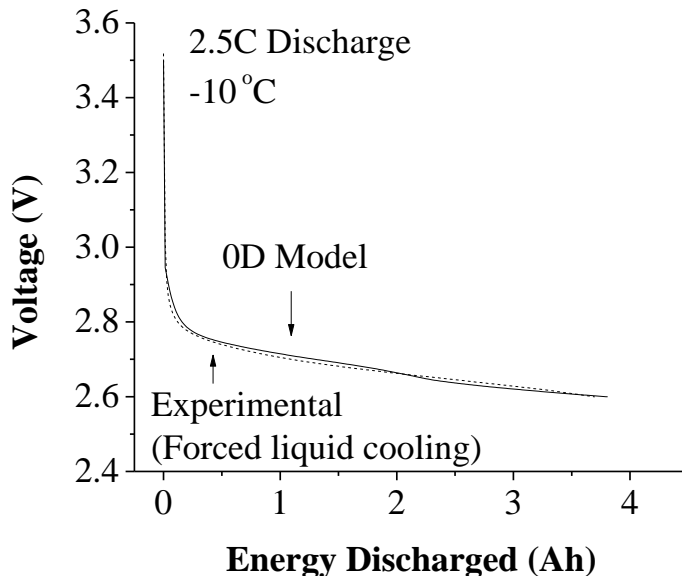
(d)
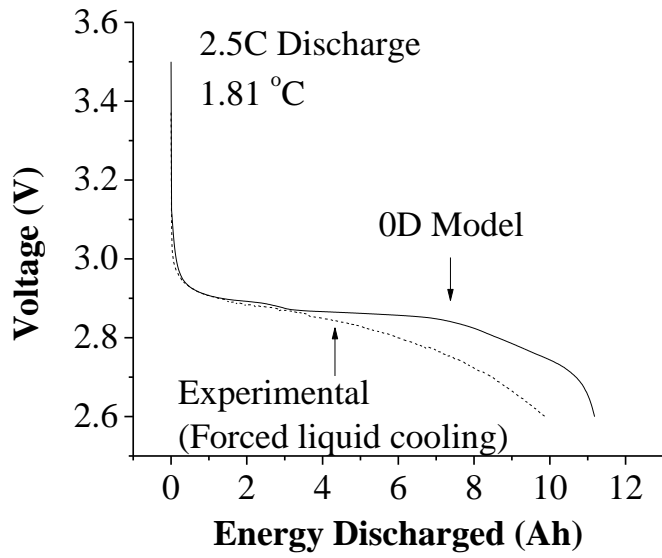
(e)
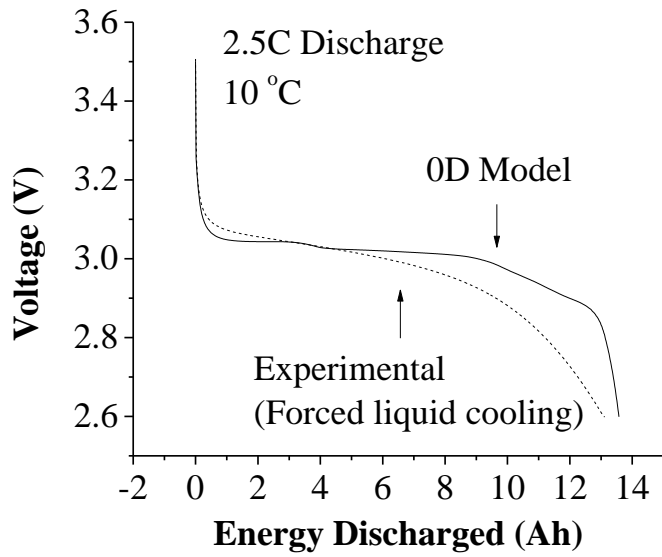
(f)
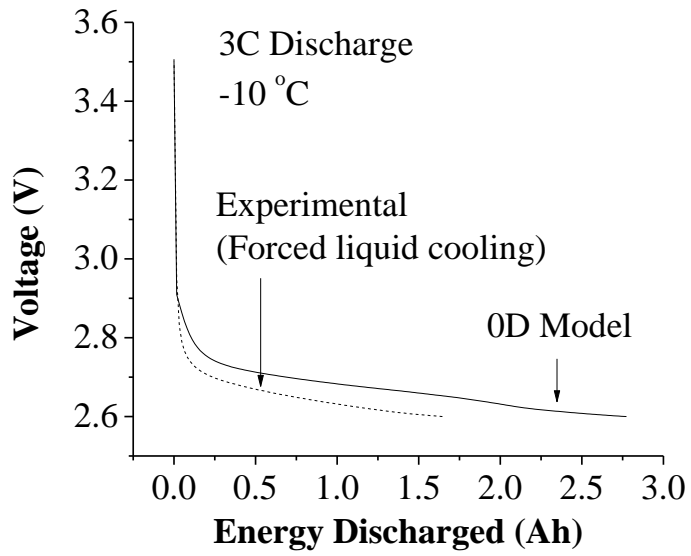
(g)
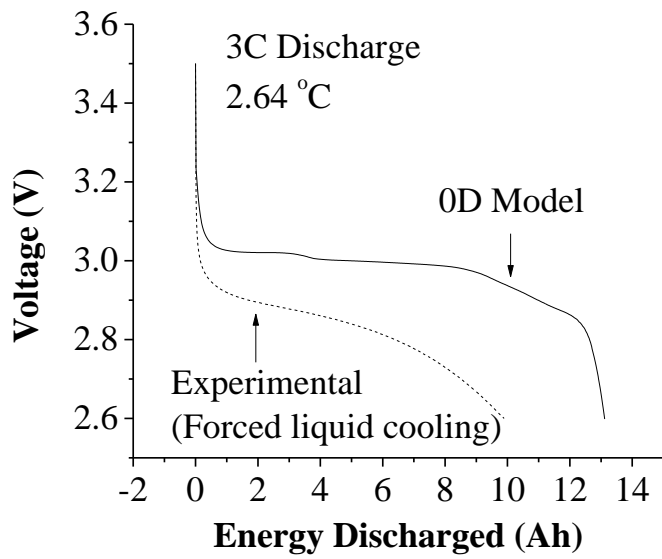
(h)
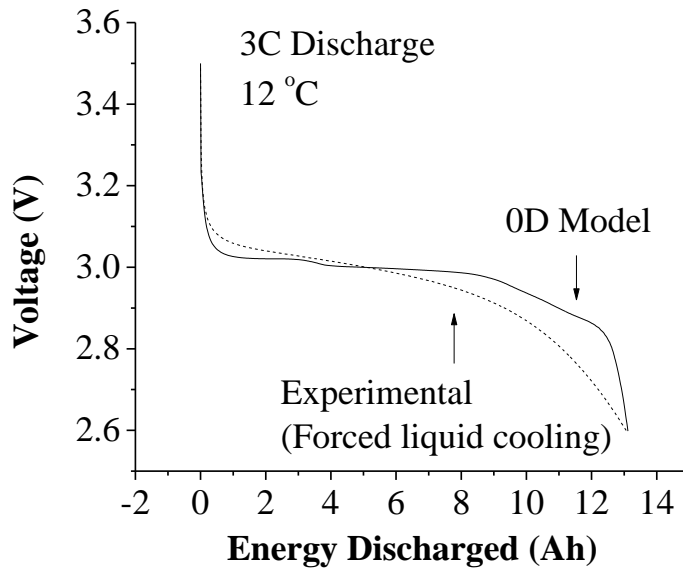
(i)

Figure 5.9: 0D model validation at various temperatures and discharge rates.

It is observed that the 0D model predicts higher voltage in the ohmic region of discharge than is observed experimentally, particularly at higher ambient temperatures. These results suggest the model under-emphasizes ohmic resistance at these ambient temperatures and discharge rates. However, there is good agreement during initial voltage drop and in the total energy discharged.

These results suggest successful validation of 0D simulations under isothermal or near-isothermal operating conditions for the purposes of this study. The notable exception is 3C discharge at subzero to near-freezing temperatures, which shows significantly higher discharge capacity than the experimental results suggest.

5.2.2 3D Model Validation

A 3D thermally-coupled electrochemical model is validated using characterization data obtained under environmental chamber conditions as described above in Section 5.1. Model setup and parameterization are described in Section 4.1. Thermal and electrochemical properties are

modeled in three dimensions as a coupled thermal-electrochemical system as described in Section 4. Simulations are run at 2C, 2.5C, and 3C, with an initial cell temperature of -10 °C and a constant ambient temperature of -10 °C, for consistency with the experimental characterization described in Section 5.1.

Validated voltage curves are shown below in Figure 5.10. It can be seen that, similar to 0D validation, the simulations predict higher voltage in the ohmic region of the discharge curves. However, reasonably similar discharge behaviour is observed between simulation and experimental results. Significant voltage drop, attributable to charge transfer resistance, occurs at the onset of discharge, followed by voltage recovery due to cell temperature rise. The cutoff voltage is reached after approximately 16.4 Ah of discharge in all cases. Table 5.5 gives the initial voltage drop and discharge capacity for both simulation and experimental results at all three C-rates, and suggests good experimental-model agreement.

The overestimation of voltage by both 0D and 3D simulation may be due in part to the model's treatment of active material diffusion in the solid and electrolyte phases. The model employs effective diffusion coefficients in solving for conservation of Li/Li$^+$ in each phase (equations 4.3 and 4.5). The coefficients are provided by the AutoLion software database and are therefore proprietary; it is not indicated how the coefficients are determined, other than that they are empirically determined for various materials. The conditions, such as temperature and lithium concentration, under which these coefficients are determined, and the range of such variables over which a given value of the coefficient is considered by the software to be assumed constant, may have significant effects on the model's output. Low temperature and strong concentration gradients for lithium in the solid and electrolyte phases reduce diffusivity. Assuming constant diffusion coefficients under such conditions has been shown to produce errors in voltage predictions of over 20% [47]. Both conditions exist for the validations performed in this thesis. Experimental cells are operating at low temperature, particularly at the onset of discharge, and for the higher C-rates used, strong concentration gradients can be expected. Such conditions, therefore, can be expected to lower diffusivity, increase concentration polarization, and reduce voltage. This may explain, in part, why initial voltage drop is lower for experimental cells, as operating temperature is at its lowest; and why model cell voltage is particularly high near the end of discharge, when cathode-side lithium concentration is significant.

Additionally, the model assumes a constant SEI layer resistance of 0.33 mΩ/m^2. However, SEI resistance has been shown to decrease with increasing temperature, while resistance values are typically determined at or near 25°C [55]. Because SEI layer resistance is known to be one of the dominant sources of overall cell resistance at subzero temperatures [3], an underestimation of SEI layer resistance at the low temperatures examined in this thesis can be expected in turn to underestimate polarization and produce higher-than-accurate voltage curves, as is seen in the above validation figures.

Thermal validation is examined both in terms of mean cell temperature rise and in terms of the development of spatial temperature distributions. Mean cell temperature rise is plotted in Figure 5.11. It can be seen at all discharge rates that the model appears to under-predict mass transport resistance, as characterized by rates of temperature rise along the corresponding region of the temperature-discharge curve. However, the overall agreement with experimental results is acceptable, with simulated and experimental mean temperature rise varying by a maximum of 10%.

Local temperature rise at the end of discharge is illustrated in Figure 5.12. The resulting temperature distribution is validated by comparing experimental local temperature rise at each thermocouple location with simulated temperature rise at the same locations. It is seen that for both model and experimental results, cell temperature rise is greatest nearest to the positive terminal, and forms a gradient of progressively lower temperature rise with distance from the positive terminal. Because the model cell assumes spatially consistent material properties, it can be inferred that, as with the experimental cell, the model cell's thermal nonuniformity is a result of spatial variations in cell resistances and the resulting feedback mechanisms between electrochemical behaviour and heat generation.

The level of agreement, however, between model and experimental results varies across the cell. Agreement is closest in the coolest regions of the cell, and increasingly diverges towards the warmest areas, with the weakest agreement near the positive terminal. This is most likely due to an underestimation by the model in joule heating by ohmic resistances. That agreement is reasonably good away from the terminals suggests that, in the absence of large ohmic losses, the model's heat generation predictions are reasonably accurate. However, at the positive terminal, where ohmic resistance is known to dominate, experimental results show significantly higher

temperature rise than the model suggests. Furthermore, in Figure 5.10, model voltage is seen to be consistently higher than experimental voltage over the ohmic polarization region of the discharge curve, again where ohmic losses are known to dominate. The thermal and voltage behaviour of the experimental cell, therefore, suggest that ohmic losses play a greater role in cell behaviour than the model represents. As ohmic losses at given location are proportional to the local current density, it is believed that the model's volume-averaged current density may be inaccurately distributed. This is identified in Section 6.2 as an area for future investigation.

Overall, however, the results suggest reasonable validation of 3D simulations for the purposes of this study, though areas for improvement are identified. The subsequent section applies both the 0D and 3D models to assess the applicability of each model to real cell behaviour, and to examine the impacts of thermal uniformity on cell performance more generally.
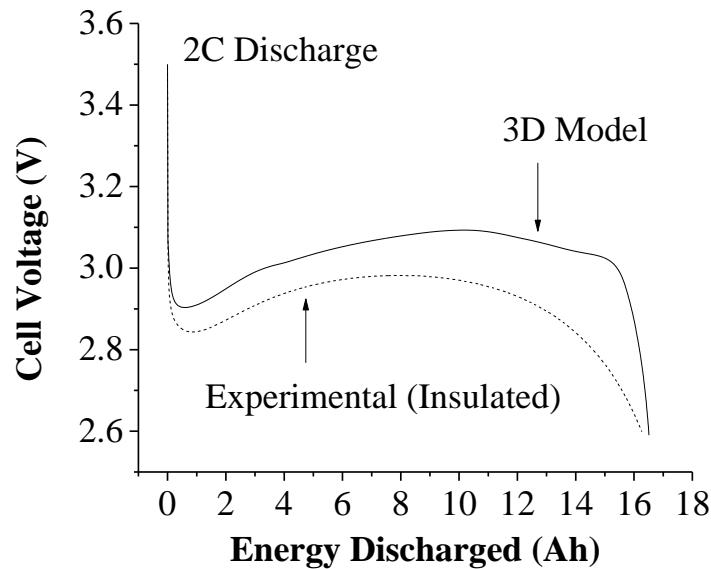
(a)
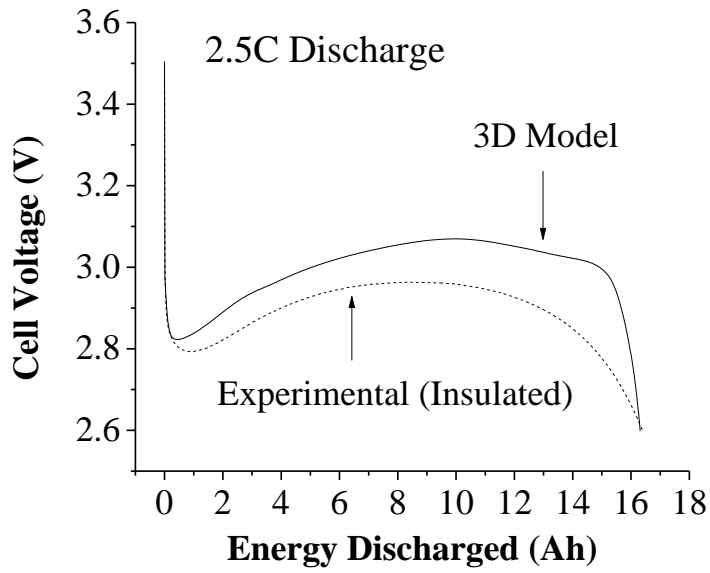
(b)
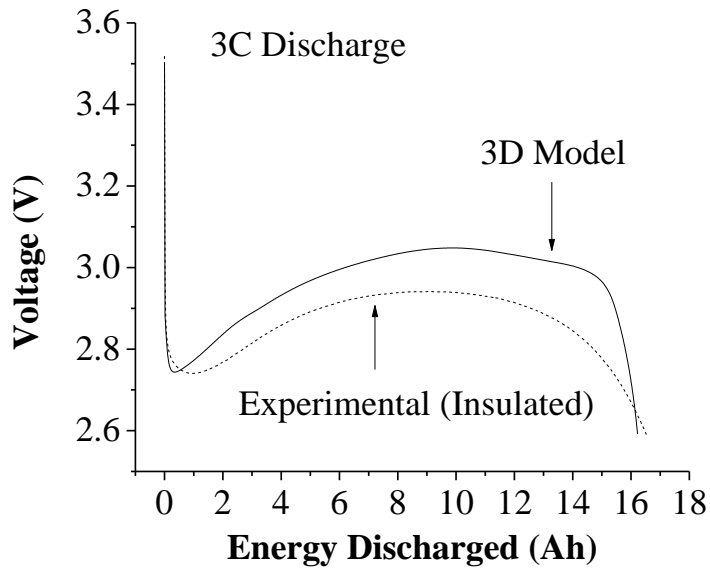
(c)

Figure 5.10: Experimental validation of 3D simulation results for cell voltage behaviour. Ambient temperature and initial cell temperature are -10 ºC.

Table 5.5: Initial voltage drop and discharge capacity for simulation and experimental results.

	Discharge Rate	Experimental	Simulation	Percent Difference (%)
Initial Voltage Drop (V)	2C	0.65	0.60	8.0
	2.5C	0.71	0.68	4.3
	3C	0.78	0.76	2.6
Discharge Capacity (Ah)	2C	16.27	16.51	1.5
	2.5C	16.40	16.31	0.6
	3C	16.48	16.22	1.6
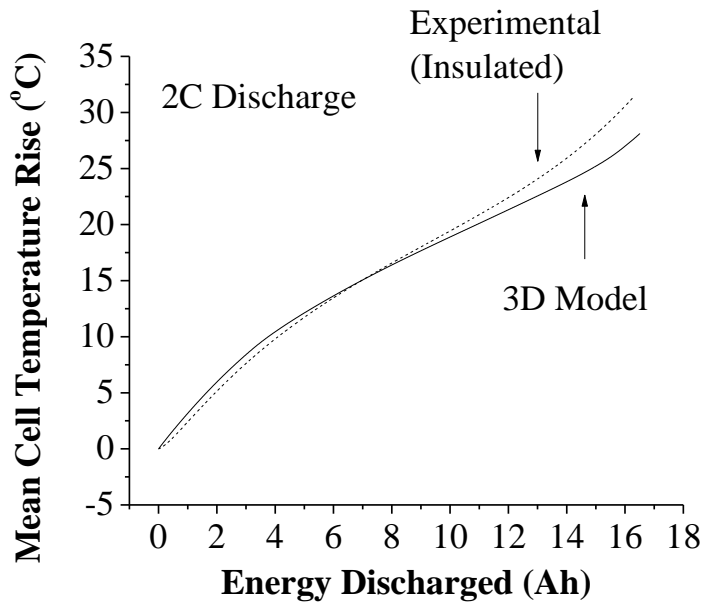
(a)
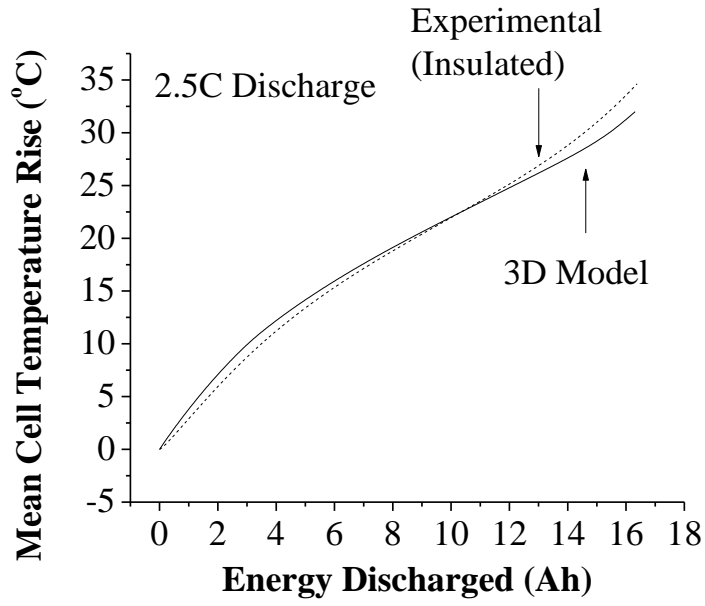
(b)
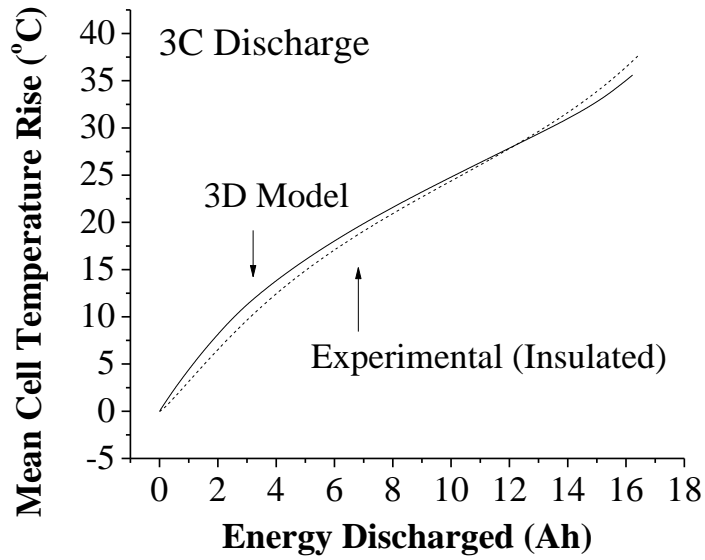
(c)

Figure 5.11: Experimental validation of 3D simulation results for mean cell temperature rise.
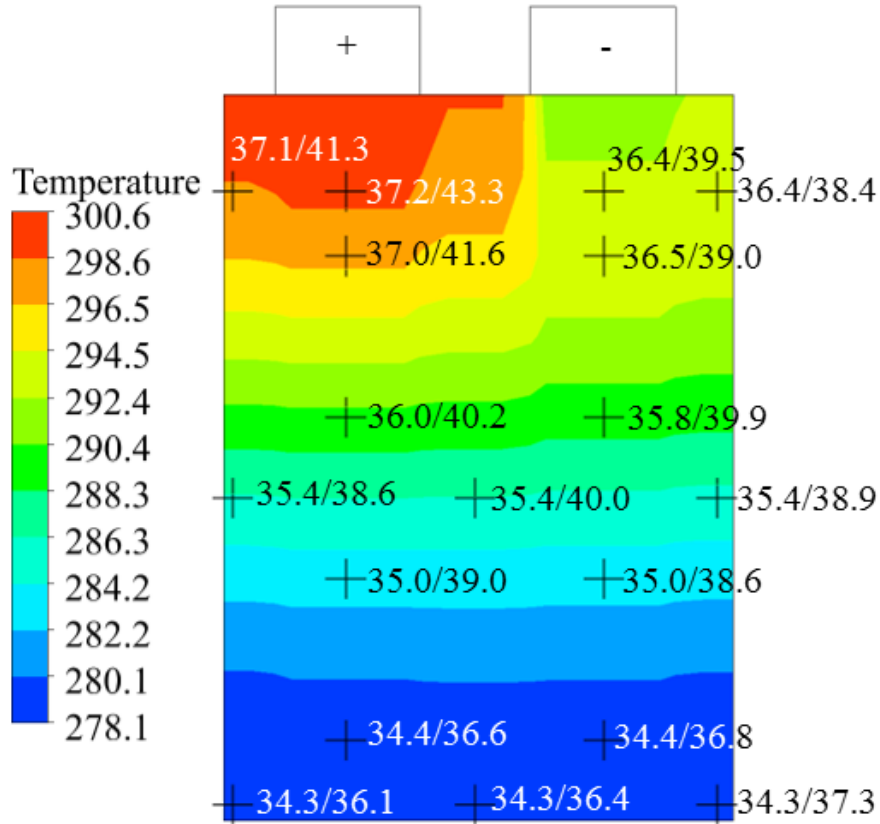
Figure 5.12: Experimental validation of 3D simulation results for local temperature rise. Contour plot shows temperature rise for 3D model at 3C discharge. Experimental temperature rise is shown for select locations. At each location, the first number shown is model temperature rise; the second is experimental. All units are in ^{o}C.

5.3   Influence of Temperature Distribution on Discharge Performance

In this section, a validated 0D isothermal model and a validated 3D thermal-electrochemical coupled model are compared in discharge performance to that of an actual battery operating at cold-start temperatures..

The 0D model represents a cell operating under thermally uniform conditions. Cell temperature rises during discharge as a result of irreversible heat generation; however, that heat is uniformly distributed throughout the cell. In other words, the cell operates at a uniform temperature at all times.

The 3D model represents a cell operating under thermally nonuniform conditions, wherein heat generation and distribution varies spatially throughout the cell. All other operating conditions are identical to the 0D model. By holding all other conditions constant and varying only the spatial resolution of heat generation and resulting temperature change, the models can be compared, and the influence of thermal uniformity on the cell's electrical performance can be observed.

Figure 5.13 compares the voltage behaviour of 0D and 3D models when operating at an ambient temperature of -10 ºC for various discharge rates. It is clearly evident that the 0D model is insufficient to describe cell voltage behaviour when discharging under cold-start conditions. It is observed that at all discharge rates, the 3D model shows greater discharge capacity; these values are compared in Table 5.6.

Additionally, voltage behaviour is notably different throughout discharge. The 0D, or thermally uniform, case shows significantly less initial voltage drop than the 3D, or thermally nonuniform, case. It can be posited that a spatially uniform temperature, and correspondingly uniform charge transfer kinetics throughout the cell, prevents the formation of areas of relatively high local charge transfer resistance which would otherwise impede the cell's overall electrochemical kinetics and induce greater voltage drop. However, this lack of localized high resistance evidently lessens internal heat generation to a sufficient extent that voltage recovery is not observed, and the cell's cutoff voltage is rapidly reached as mass transfer resistance dominates at the cathode.
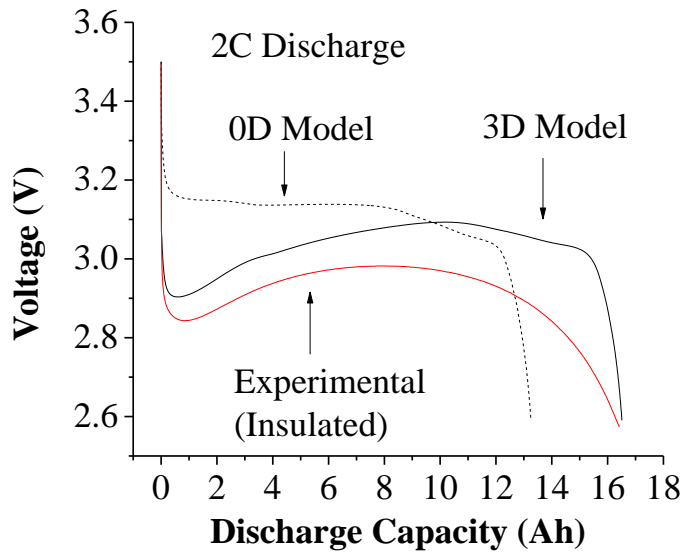
(a)
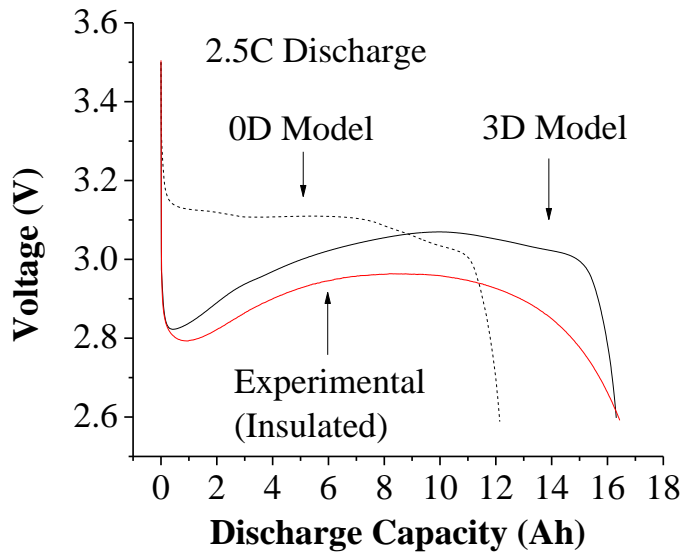
(b)
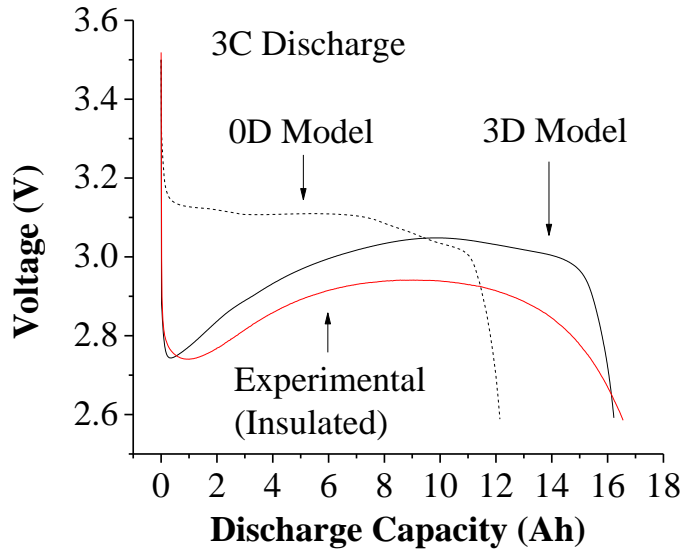
(c)

Figure 5.13: Voltage behaviour of 0D and 3D thermally coupled models when operating at an ambient temperature and initial temperature of -10 $^\circ$C and a heat transfer coefficient of $h = 0.47$ Wm^{-2}K^{-1}, for various discharge rates. Experimental curves derived under identical conditions are shown for comparison.

Table 5.6: Discharge capacity predicted by 0D and 3D models under identical operating conditions.

	Discharge Rate	0D Model	3D Model	Percent Difference (%)
	2C	13.25	16.51	24.6
Discharge Capacity (Ah)	2.5C	12.14	16.31	34.3
	3C	12.02	16.22	34.9

6   Conclusions and Recommendations

6.1   Conclusions

In this thesis, an electrochemical cell model coupled to either a 0D or 3D thermal model is validated to assess the suitability of each thermal model to describe the performance of prismatic LiFePO$_4$ Li-ion batteries under cold-start conditions. The investigation is composed of three parts. First, the electrical and thermal behaviour of the cell is characterized under different heat transfer conditions and at various discharge rates and ambient temperatures. It is shown that under conditions where rates of heat removal and mixing in the environment around the cell are low, temperature rise is rapid at the onset and end of discharge, voltage recovery provides greater discharge capacity, and changes in temperature are nonuniform throughout the cell.   Under conditions where the cell temperature is held effectively constant and uniform at low temperatures, conversely, electrical performance deteriorates.

The second part of the investigation applies the results of the first to a validation of a 0D lumped capacitance thermal model and a fully 3D thermal model. It is shown that good agreement is achieved for global temperature and voltage under the 3D model at all discharge rates, with a maximum variance in discharge capacity of 1.6% and a maximum mean temperature variance of 10%. Similarly good agreement is achieved for the 0D model at 2C and 2.5C discharge. In general, however, the model over-predicts discharge voltage during mid- to late-discharge. This disagreement is attributed to three main factors. First, the assumption of a constant solid-state diffusion coefficient, D_s, neglects the sensitivity of solid-state diffusion to low temperature and to the presence of strong Li concentration gradients, both of which are significant during the high-rate discharge and subzero temperatures characteristic of cold-start EV driving. Second, the model's assumption of a constant SEI layer resistance, R_f, implies that the empirically-determined SEI layer resistance value holds across a wide temperature range; however, it is known that SEI layer resistance increases at low temperature. Third, disagreement in the region of the voltage curve where ohmic resistance is known to dominate, as well as in local temperature near the terminals where ohmic resistance again dominates, suggests inaccuracies in the model's predictions of current density distribution.

66

The third part of the investigation directly compares the results of the 0D and 3D models under identical discharge scenarios. It is observed that the 0D lumped thermal capacitance model is insufficient for describing the discharge behaviour of prismatic batteries under cold-start conditions. These results suggest that for thermally nonuniform cells operating at subzero ambient temperatures, the formation of temperature gradients, and therefore of areas of high and low local resistance, cannot be neglected for its influence on overall cell voltage. Moreover, these results are in contrast to commonly held assumptions in the literature that a more thermally uniform cell should perform better and provide greater discharge capacity as a product of evenly distributed reactions across the electrode, consistent charge density, and uniform SOC. Instead, the results of this thesis suggest that, under subzero conditions, cells that experience local temperature minima experience sufficiently high local internal resistance so as to significantly affect the temperature-resistance-voltage feedback cycle for the cell overall, reducing internal resistance in the late stages of discharge and ultimately increasing discharge capacity. The results provide insight into the significance of temperature gradients and their effects on prismatic battery performance under cold-start conditions, and illustrate the need to further refine models that are capable of describing the effects of these gradients under such conditions.

6.2 Recommendations

Based on the above conclusions, the following recommendations are made:

1. The design, modeling, and application of large prismatic cells and batteries should not neglect the formation of, and effect of, strong temperature gradients during cold-start operation.
2. Models of large prismatic cells and batteries during cold-start operation should employ a 3D thermally-coupled electrochemical approach that discretizes temperature throughout the cell, capturing the spatial thermal behaviour and its effects on local and global electrochemical feedback loops.
3. The model's solid-state diffusion coefficient, D_s, should be treated as a function of temperature and discharge rate to reflect actual transport properties during cold-start discharge in a real cell. Currently, D_s is treated by the model as a constant and does not

account for the lower rates of solid-state diffusion experienced in cells at subzero temperatures and at high discharge rates, where strong concentration gradients impede diffusion. Application of a function that calculates D_s at each time step based on temperature and lithium concentration should improve the accuracy of discharge voltage prediction, particularly late in the discharge curve.

4. The model's SEI layer resistance, R_f, should be treated as a function of temperature. The empirically-determined SEI layer resistance value employed in the model is assumed constant, whereas SEI layer resistance in a real cell increases with decreasing temperature. Calculation of R_f at each time step as a function of temperature, or use of a database of constant R_f values, each of which pertains to a specific range of cell local cell temperature, should provide greater accuracy in predicting discharge voltage.

5. Current density distributions should be validated for the 3D model. Validation of discharge voltage and local temperature rise suggests that local current density, and the resulting ohmic losses and associate heat generation, are not in good agreement with experimental results where ohmic losses dominate. Current density distributions should be experimentally validated to determine whether model inaccuracies in current density are at the root of weak agreement in local heat generation at the terminals and in voltage at moderate SOC.

6. Future model validation should be broadened to include other cell materials. A cell's composition, including but not limited to its electrode and electrolyte materials and physicochemical properties, affects the relative and absolute magnitude of its internal resistances and therefore the cell's sensitivity to temperature. As existing cell chemistries are improved and new materials are introduced, the electrochemical-thermal feedback behaviour of new cells will differ from that observed here, and accurate characterization and validation will be required to adapt models accordingly.

References

1.   Dinger, A., et al., *Batteries for electric cars: Challenges, opportunities, and the outlook to 2020.* The Boston Consulting Group, 2010: p. 18.

2.   Ji, Y., Y. Zhang, and C.-Y. Wang, *Li-Ion Cell Operation at Low Temperatures.* Journal of the Electrochemical Society, 2013. **160**(4): p. A636-A649.

3.   Nagasubramanian, G., *Electrical characteristics of 18650 Li-ion cells at low temperatures.* Journal of Applied Chemistry, 2001. **31**: p. 99-104.

4.   Zhang, S.S., K. Xu, and T.R. Jow, *Low-temperature performance of Li-ion cells with a LiBF4-based electrolyte.* Journal of Solid State Electrochemistry, 2003. **7**: p. **147-151**.

5.   Zhang, Y., C.-Y. Wang, and X. Tang, *Cycling degradation of an automotive LiFePO4 lithium-ion battery.* Journal of Power Sources, 2011. **196**: p. 1513-1520.

6.   Andre, D., et al., *Characterization of high-power lithium-ion batteries by electrochemical impedance spectroscopy. I. Experimental investigation.* Journal of Power Sources, 2011. **196**(5334-5341).

7.   Bandhauer, T.M., S. Garimella, and T.F. Fuller, *A critical review of thermal issues in Lithium-ion batteries.* Journal of the Electrochemical Society, 2011. **158**(3): p. R1-R25.

8.   *FreedomCAR Battery Test Manual, Revision 3*. 2003.

9.   *Handbook of Batteries*, D. Linden and T.B. Reddy, Editors. 2002, McGraw-Hill.

10.   Lin, C., et al., *Research on thermo-physical properties identification and thermal analysis of EV Li-ion battery*, in *Vehicle Power and Propulsion Conference*. 2009, IEEE. p. 1643-1648.

11.   Pals, C.R. and J. Newman, *Thermal modeling of the lithium/polymer battery. I. Discharge behaviour of a single cell.* Journal of the Electrochemical Society, 1995. **142**(10): p. 3274-3281.

12.   Pals, C.R. and J. Newman, *Thermal modeling of the lithium/polymer battery. II. Temperature profiles in a cell stack.* Journal of the Electrochemical Society, 1995. **142**(10): p. 3282-3288.

13.   Yang, K., J.J. An, and S. Chen, *Temperature characterization analysis of LieFePO4/C power battery during charing and discharging.* Journal of Thermal Analysis and Calorimetry, 2010. **99**: p. 515-521.

14.   Gu, W.B. and C.Y. Wang, *Thermal-electrochemical modeling of battery systems.* Journal of the Electrochemical Society, 2000. **147**(8): p. 2910-2922.

15.   Kim, U.S., C.B. Shin, and C.-S. Kim, *Effect of electrode configuration on the thermal behavior of a lithium-polymer battery.* Journal of Power Sources, 2008. **180**(909-916).

16.   Kim, U.S., C.B. Shin, and C.-S. Kim, *Modeling for the scale-up of a lithium-ion polymer battery.* Journal of Power Sources, 2009. **189**: p. 841-846.

17.   Wu, W., X. Xiao, and X. Huang, *The effect of battery design parameters on heat generation and utilization in a Li-ion cell.* Electrochimica Acta, 2012. **83**: p. 227-240.

18.   Chen, Y. and J.W. Evans, *Heat transfer phenomena in Lithium/polymer-electrolyte batteries for electric vehicle application.* Journal of the Electrochemical Society, 1993. **140**(7): p. 1833-1838.

19.   Zhang, S.S., K. Xu, and T.R. Jow, *The low temperature performance of Li-ion batteries.* Journal of Power Sources, 2003. **115**: p. 137-140.

20.	Lin, C., et al., *Thermal analysis of large-capacity LiFePO₄ power batteries for electric vehicles.* Journal of Power Sources, 2015. **294**: p. 633-642.

21.	Smart, M.C., B.V. Ratnakumar, and S. Surampudi, *Electrolytes for low-temperature Lithium batteries based on ternary mixtures of aliphatic carbonates.* Journal of the Electrochemical Society, 1999. **146**(2): p. 486-492.

22.	Plichta, E.J. and W.K. Behl, *A low-temperature electrolyte for Lithium and Lithium-ion batteries.* Journal of Power Sources, 2000. **88**: p. 192-196.

23.	Ratnakumar, B.V., M.C. Smart, and S. Surampudi, *Effects of SEI on the kinetics of Lithium interacalation.* Journal of Power Sources, 2001. **97-98**: p. 137-139.

24.	Huang, C.-K., et al., *The limits of low-temperature performance of Li-ion cells.* Journal of the Electrochemical Society, 2000. **147**(8): p. 2893-2896.

25.	Zhang, S.S., K. Xu, and T.R. Jow, *Low temperature performance of graphite electrode in Li-ion cells.* Electrochimica Acta, 2002. **48**: p. 241-246.

26.	Jansen, A.N., et al., *Low-temperature study of lithium-ion cells using a Li_ySn micro-reference electrode.* Journal of Power Sources, 2007. **174**: p. 373-379.

27.	Abraham, D.P., et al., *Investigating the low-temperature impedance increase of lithium-ion cells.* Journal of the Electrochemical Society, 2008. **155**(1): p. A41-A47.

28.	Jow, T.R., M.B. Marx, and J.L. Allen, *Distinguishing Li⁺ charge transfer kinetics at NCA/electrolyte and graphite/electrolyte Interfaces, and NCA/electrolyte and LFP/electrolyte interfaces in Li-ion cells.* Journal of the Electrochemical Society, 2012. **159**(5): p. A604-A612.

29.	Chen, K. and X. Li, *Accurate determination of battery discharge characteristics - A comparison between two battery temperature control methods.* Journal of Power Sources, 2014. **247**: p. 961-966.

30.	Choi, S.S. and H.S. Lim, *Factors that affect cycle-life and possible degradation mechanisms of a Li-ion cell based on LiCoO₂.* Journal of Power Sources, 2002. **111**: p. 130-136.

31.	Awarke, A., et al., *Thermal analysis of a Li-ion battery module under realistic EV operating conditions.* Internal Journal of Energy Research, 2013. **37**: p. 617-630.

32.	Bernardi, D., E. Pwlikowski, and J. Newman, *A general energy balance for battery systems.* Journal of the Electrochemical Society, 1985. **132**(1): p. 5-12.

33.	Chen, K., G. Unsworth, and X. Li, *Measurements of heat generation in prismatic Li-ion batteries.* Journal of Power Sources, 2014. **261**: p. 28-37.

34.	Wang, C.Y. and V. Srinivasan, *Computational battery dynamics (CBD) - electrochemical/thermal coupled modeling and multi-scale modeling.* Journal of Power Sources, 2002. **110**: p. 364-376.

35.	Arora, S., W. Shen, and A. Kapoor, *Neural network based computational model for estimation of heat generation in LiFePO₄ pouch cells of different nominal capacities.* Computers and Chemical Engineering, 2017. **101**: p. 81-94.

36.	Inui, Y., et al., *Simulation of temperature distribution in cylindrical and prismatic lithium ion secondary batteries.* Energy Conversion and Management, 2007. **48**: p. 2103-2109.

37.	Chen, S.C., C.C. Wan, and Y.Y. Wang, *Thermal analysis of lithium-ion batteries.* Journal of Power Sources, 2005. **140**: p. 111-124.

38.	Keyser, M.A., et al., *Thermal characterization of advanced Lithium-ion polymer cells*, in *Third Advanced Automotive Battery Conference*. 2003.

39. Fleckenstein, M., et al., *Current density and state of charge inhomogeneities in Li-ion battery cells with LiFePO4 as cathode material due to temperature gradients.* Journal of Power Sources, 2011. **196**(4769-4778).

40. Doyle, M., T.F. Fuller, and J. Newman, *Modeling of galvanostatic charge and discharge of the Lithium/polymer/insertion cell.* Journal of the Electrochemical Society, 1993. **140**(6): p. 1526-1533.

41. Fuller, T.F., M. Doyle, and J. Newman, *Simulation and optimization of the dual Lithium ion insertion cell.* Journal of the Electrochemical Society, 1994. **141**(1): p. 1-10.

42. Doyle, M., et al., *Comparison of modeling predicitons with experimental data from plastic Lithium ion cells.* Journal of the Electrochemical Society, 1996. **143**(6): p. 1890-1903.

43. Al-Hallaj, S. and J.R. Selman, *Thermal modeling of secondary lithium batteries for electric vehichle/hybrid electric vehicle applications.* Journal of Power Sources, 2002. **110**: p. 341-348.

44. Smith, K. and C.-Y. Wang, *Power and thermal characterization of a Lithium-ion battery pack for hybrid-electric vehicles.* Journal of Power Sources, 2006. **160**: p. 662-673.

45. Song, L. and J.W. Evans, *Electrochemical-thermal model of Lithium polymer batteries.* Journal of the Electrochemical Society, 2000. **147**(6): p. 2086-2095.

46. Kwon, K.H., et al., *A two-dimensional modeling of a Lithium-polymer battery.* Journal of Power Sources, 2006. **163**: p. 151-157.

47. Fan, G., et al., *Modeling of Li-ion cells for fast simulation of high C-rate and low temperature operations.* Journal of the Electrochemical Society, 2016. **163**(5): p. A666-A676.

48. Hong, J.-S., et al., *Electrochemical-calorimetric studies of Lithium-ion cells.* Journal of the Electrochemical Society, 1998. **145**(5): p. 1489-1507.

49. (2014) *AutoLion 3D User's Manual version 3.2.4a.* 78.

50. Gu, W.B. and C.Y. Wang. *Thermal-electrical coupled modeling of a lithium-ion cell.* in *Proceedings of the ECS.* 2000.

51. Fang, W., O.J. Kwon, and C.-Y. Wang, *Electrochemical-thermal modeling of automotive Li-ion batteries and experimental validation using a three-electrode cell.* Internal Journal of Energy Research, 2009. **34**: p. 107-115.

52. Ji, Y., *Low-temperature operation of Li-ion batteries for hybrid and electric vehicles.* 2014. p. 168.

53. Chen, Y. and J.W. Evans, *Thermal analysis of Lithium-ion batteries.* Journal of the Electrochemical Society, 1996. **143**(9): p. 2708-2712.

54. D'Errico, J. *Surface Fitting using gridfit -* http://www.mathworks.com/matlabcentral/fileexchange/8998-surface-fitting-using-gridfit [cited 2015.

55. Benitez, L. and J.M. Seminario, *Ion diffusivity through the solid electrolyte interphase in lithium-ion batteries.* Journal of the Electrochemical Society, 2017. **164**(11): p. E3159-E3170.

Appendix I: Model Cell Design Parameters

Property	Value	Units
Dimensions		
Cell Width	160	mm
Cell Height	227	mm
Cell Thickness	7.25	mm
Enclosure Weight	6.21	g
Positive Electrode Assembly - Foil		
Material	Al	N/A
Thickness	15	μm
Width	160	mm
Density	2.7	g/cm^3
Conductivity	3.538E+7	S/m
Positive Electrode Assembly – Active Material		
Material	LFPO	N/A
Molecular Weight	157.751	g/mol
Density	3.6	g/cm^3
1st Charge Capacity	160	mAh/g
1st Discharge Capacity	150	mAh/g
Cutoff voltage for reversible specific capacity	3.8	V

Particle Diameter	0.104	µm
Weight Percentage	94	%

Positive Electrode Assembly – Conductive Agent

Material	Carbon	N/A
Density	1.95	g/cm^3
Weight Percentage	3	%

Positive Electrode Assembly – Binder

Material	PVdF	N/A
Density	1.77	g/cm^3
Weight Percentage	3	%

Positive Electrode Assembly – Additive

Weight Percentage	0	%

Positive Electrode Assembly – Coating

Loading	1.6	mAh/cm^2
Electrode Thickness	170	µm
Electrode Width	160	mm
Electrode Height	227	mm
# of Electrode Plates	18	N/A

<u>Positive Electrode Assembly - Summary</u>

Total Coated Area	13,075.2	cm^2
Porosity	0.6	N/A
Mass Loading	10.6383	mg/cm^2

Dry Electrode Density	1.37	g/cm^3
Active Material Used	130.752	g

Negative Electrode Assembly - Foil

Material	Cu	N/A
Thickness	8	μm
Width	160	mm
Density	8.96	g/cm^3
Conductivity	5.8E+7	S/m

Negative Electrode Assembly – Active Material

Material	Graphite	N/A
Molecular Weight	72.06	g/mol
Density	2.24	g/cm^3
1st_Charge_Capacity	371.933	mAh/g
1st_Discharge_Capacity	365	mAh/g
Cutoff voltage for reversible specific capacity	2	V
Particle Diameter	15	μm
Weight Percentage	94	%

Negative Electrode Assembly – Conductive Agent

Material	Carbon	N/A
Density	1.95	g/cm^3
Weight Percentage	3	%

Negative Electrode Assembly – Binder

Material	PVdF	N/A
Density	1.77	g/cm^3
Weight Percentage	3	%
Negative Electrode Assembly – Additive		
Weight Percentage	0	%
Negative Electrode Assembly – Coating		
N/P Ratio	115	%
Loading	1.84	mAh/cm^2
Electrode Thickness	170	µm
Electrode Width	160	mm
Electrode Height	227	mm
# of Electrode Plates	19	N/A
<u>Negative Electrode Assembly – Summary</u>		
Total Coated Area	13,801.6	cm^2
Porosity	0.71	N/A
Mass Loading	5.2629	mg/cm^2
Dry Electrode Density	0.65	g/cm^3
Active Material Used	68.278	g
Separator		
Type	Celgard	N/A
Thickness	20	um
Density	1.2	g/cm^3

Height	227	mm
Porosity	0.8	N/A
Electrolyte		
Lithium Salt	$LiPF_6$	N/A
Solution	EC-EMC-DMC	N/A
Concentration	1.2	mol/L
Density	1.2	g/cm^3

Appendix II: Simulation Parameters

Property	Value	Units
Control Parameters		
Time Step Size	1	s
Output Frequency	50	s^{-1}
Mesh Number		
Negative Electrode	8	Control Volumes
Separator	5	Control Volumes
Positive Electrode	8	Control Volumes
Operating Conditions		
Lower Cutoff Voltage	2.6	V
Upper Cutoff Voltage	3.65	V
Load Profiles	C-rate	N/A
C-rate	2, 2.5, 3	C
Initial Conditions		
OCV@100%SOC	3.55	V
SOC	1	N/A
Butler-Volmer Equation – Negative Electrode		
Open Circuit Potential	database	V
Anodic Transfer Coefficient	0.5	N/A
Cathodic Transfer Coefficient	0.5	N/A

Exchange Current Density	database	A/m^2
SEI Layer Resistance Reference Value	0.00033	Ohm m^2
SEI Layer Resistance Activation Energy	3.2E+4	J/mol
dU/dT Entropic Heat	database	V/K

Butler-Volmer Equation –Positive Electrode

Open Circuit Potential	database	V
Anodic Transfer Coefficient	0.5	N/A
Cathodic Transfer Coefficient	0.5	N/A
Exchange Current Density	database	A/m^2
Film Resistance Reference Value	0	Ohm m^2
Film Resistance Activation Energy	3.2E+4	J/mol
dU/dT Entropic Heat	database	V/K

Bruggeman Exponents

Negative Electrode	1.5	N/A
Separator	1.5	N/A
Positive Electrode	1.5	N/A

Electrolyte Concentration

Average Concentration	1200	mol/m3
Diffusion Coefficient	database	m^2/s
Transference Number	0.38	N/A

Electrolyte Potential

Ionic Conductivity	database	S/m

Diffusional Conductivity	database	A/m

Solid Phase Potential – Negative Electrode

Conductivity	100	S/m
Contact Resistance	0.0002	Ohm m^2

Solid Phase Potential – Positive Electrode

Conductivity	3.8	S/m
Contact Resistance	0.0002	Ohm m^2

Mesh Generation

Width Mesh	6	mm
Height Mesh	9	mm
Negative Tab Location	2	N/A
Negative Htab Value	27	mm
Negative Htab Mesh	3	mm
Negative Wtab Value	45	mm
Negative Dtab Value	18	mm
Positive Tab Location	2	N/A
Positive Htab Value	27	mm
Positive Htab Mesh	3	mm
Positive Wtab Value	45	mm
Positive Dtab Value	97	mm